

TOPICAL REVIEW • OPEN ACCESS

Solution-processing approach of nanomaterials toward an artificial sensory system

To cite this article: Okin Song *et al* 2024 *Int. J. Extrem. Manuf.* **6** 052001

View the [article online](#) for updates and enhancements.

You may also like

- [Device design principles and bioelectronic applications for flexible organic electrochemical transistors](#)
Lin Gao, Mengge Wu, Xinge Yu et al.
- [CMOS-compatible neuromorphic devices for neuromorphic perception and computing: a review](#)
Yixin Zhu, Huiwu Mao, Ying Zhu et al.
- [The role of stimulus periodicity on spinal cord stimulation-induced artificial sensations in rodents](#)
Jacob C Slack, Sidnee L Zeiser and Amol P Yadav

Topical Review

Solution-processing approach of nanomaterials toward an artificial sensory system

Okin Song^{1,3} , Youngwook Cho^{2,3} , Soo-Yeon Cho^{2,*}  and Joohoon Kang^{1,*} 

¹ School of Advanced Materials Science and Engineering, Sungkyunkwan University (SKKU), Suwon 16419, Republic of Korea

² School of Chemical Engineering, Sungkyunkwan University (SKKU), Suwon 16419, Republic of Korea

E-mail: sooyeonc@skku.edu and joohoon@skku.edu

Received 21 February 2024, revised 26 March 2024

Accepted for publication 14 May 2024

Published 31 May 2024



CrossMark

Abstract

Artificial sensory systems have emerged as pivotal technologies to bridge the gap between the virtual and real-world, replicating human senses to interact intelligently with external stimuli. To practically apply artificial sensory systems in the real-world, it is essential to mass-produce nanomaterials with ensured sensitivity and selectivity, purify them for desired functions, and integrate them into large-area sensory devices through assembly techniques. A comprehensive understanding of each process parameter from material processing to device assembly is crucial for achieving a high-performing artificial sensory system. This review provides a technological framework for fabricating high-performance artificial sensory systems, covering material processing to device integrations. We introduce recent approaches for dispersing and purifying various nanomaterials including 0D, 1D, and 2D nanomaterials. We then highlight advanced coating and printing techniques of the solution-processed nanomaterials based on representative three methods including (i) evaporation-based assembly, (ii) assisted assembly, and (iii) direct patterning. We explore the application and performances of these solution-processed materials and printing methods in fabricating sensory devices mimicking five human senses including vision, olfaction, gustation, hearing, and tactile perception. Finally, we suggest an outlook for possible future research directions to solve the remaining challenges of the artificial sensory systems such as ambient stability, device consistency, and integration with AI-based software.

Keywords: artificial sensory system, nanomaterials, solution-processing, printing, sensor

³ These authors contributed equally to this work.

* Authors to whom any correspondence should be addressed.



Original content from this work may be used under the terms of the [Creative Commons Attribution 4.0 licence](https://creativecommons.org/licenses/by/4.0/). Any further distribution of this work must maintain attribution to the author(s) and the title of the work, journal citation and DOI.

1. Introduction

With the emphasis on the era of data conversion between virtuality and reality to achieve artificial intelligence (AI), artificial sensory technology is critical to provide objective sensing and intelligent feedback capabilities from the real-world that mimic five human sensing ability including vision, smell, taste, hearing, and touch to external stimuli [1–8]. Artificial sensory systems consist of perceptual interfaces that systematically detect external stimuli and a process of digitizing them, expanding the capabilities of biological senses by integrating advanced sensing technologies, signal transmission, and intelligent algorithms [1, 9–12]. With continued research and development on related fields ranging from materials, systems, to data processing [1, 13, 14], this convergent technology is expected to enhance and link biological sensory systems with the environment for applications such as digital healthcare [15–17], smart robots [18, 19], and smart agriculture [20–22].

Artificial sensory devices mimic five human senses by following stimuli conversion [18], signal transmission by artificial nervous systems [10], signal fusion [9], and digital recognition mechanisms [11, 19]. To achieve this, nanoscale transducer materials with tailored structural and functional surface characteristics have been integrated with sensing devices based on their superior sensitivity and selectivity to specific stimuli [23–26]. Versatile dimensions of nanoscale materials including zero-dimensional (0D), one-dimensional (1D), and two-dimensional (2D) structures, have been widely used to convert the external stimuli due to their tunable energy bandgap, large active area for sensing, and superior sensitivity. They offer tunable bandgaps based on their distinct structural parameters such as lateral dimensions, grain size, and layer thickness, thereby controlling the electronic potentials of devices and broadening the spectrum of detectable senses [25, 27–29]. In addition, nanoscale materials can be used as highly sensitive sensing channels of the artificial sensory devices since their surface-to-volume ratio is maximized and electron/hole transport of a device is confined, making them extremely sensitive and fast responding to external stimuli [23, 24, 30]. The environments where artificial sensory systems are deployed require the conversion of a wide and sensitive range of instantaneous physical stimuli from real-world [1, 18, 31], making nanomaterials with these two characteristics top candidates.

Beyond enhancing sensing performance, nanomaterials also offer the benefit of compatibility with large-area fabrication processes. Unlike conventional sensor devices, artificial sensory systems need to be fabricated in sizes and volumes similar to human sensory organs having millimeter to centimeter scale to convert real-world stimulation, necessitating their capability for large-area device fabrication [32–34]. In this regard, solution-based processing of nanomaterials offers a straightforward, cost-effective, and scalable approach for fabricating artificial sensory system [35, 36] due to their easy and stable dispersion in various type of processing solvents

[37–39], which is hard to be achieved with a traditional solid-phase materials synthesis and preparation process such as mechanical exfoliation or chemical vapor deposition [39]. To enhance the sensing capabilities of artificial sensory systems, it is crucial to minimize well-known size effects of nanoscale materials by precise selection of nanomaterials through a systematic purification process (e.g. density gradient ultracentrifugation) based on their structure, size, and density [40–42]. The integration of the resulting dispersion-based nanomaterials has been achieved by three representative processes: evaporation-based assembly, assisted assembly, and direct patterning [36, 39]. Specific processes for different sensory types may be adopted, thereby producing highly sensitive, selective, and reliable sensing channel constructs that play a key role in the artificial sensory system. Many recent studies highlight the practical applications of the artificial sensory devices that integrate low-dimensional nanomaterials sensory elements produced through coating or printing processes [25, 28, 36].

As these crucial technologies have been being developed, there have been many reviews on artificial sensory applications and technologies [1, 4, 23–25]. However, comprehensive reviews covering the whole process from nanomaterial preparation through solution-processing to device integration for artificial sensory systems are lacking. By addressing the synthesis and purification of nanomaterials, exploring coating/printing-based solution-processes, and evaluating performance, artificial sensory technology can be effectively integrated into broad-spectrum real-world applications with high-performances.

In this review, we provide a comprehensive design rule for high-performance artificial sensory systems from material selection to device fabrication step (figure 1). We first introduce the synthesis and dispersion method of 0D (e.g. nanoparticle and quantum dot (QD)), 1D (e.g. nanotube, nanorod, and nanowire (NW)), and 2D (e.g. graphene, transition metal dichalcogenide, or black phosphorus (BP)) nanomaterial candidates for the artificial sensory devices and their solution-based post-processing technique for the purification. Next, we will summarize the representative coating/printing technique recently developed based on evaporation-based assembly (drop casting, spin coating, spray coating, and dip coating), assisted assembly (Langmuir–Blodgett (LB) and Langmuir–Schaefer (LS)), and direct patterning (3D printing and inkjet printing) category. The implementation and real-world performances of artificial sensory devices based on the five human senses (e.g. artificial retina (vision), Electronic (E)-nose (smell), E-tongue (taste), artificial basilar membrane (ABM) (hearing), and E-skin (touch)), assembled via coating/printing process are also introduced. Finally, we suggest an outlook on the current technological challenges in artificial sensory systems related to ambient stability, minimizing device-to-device variation, and integrating AI-based machine learning software and systems.

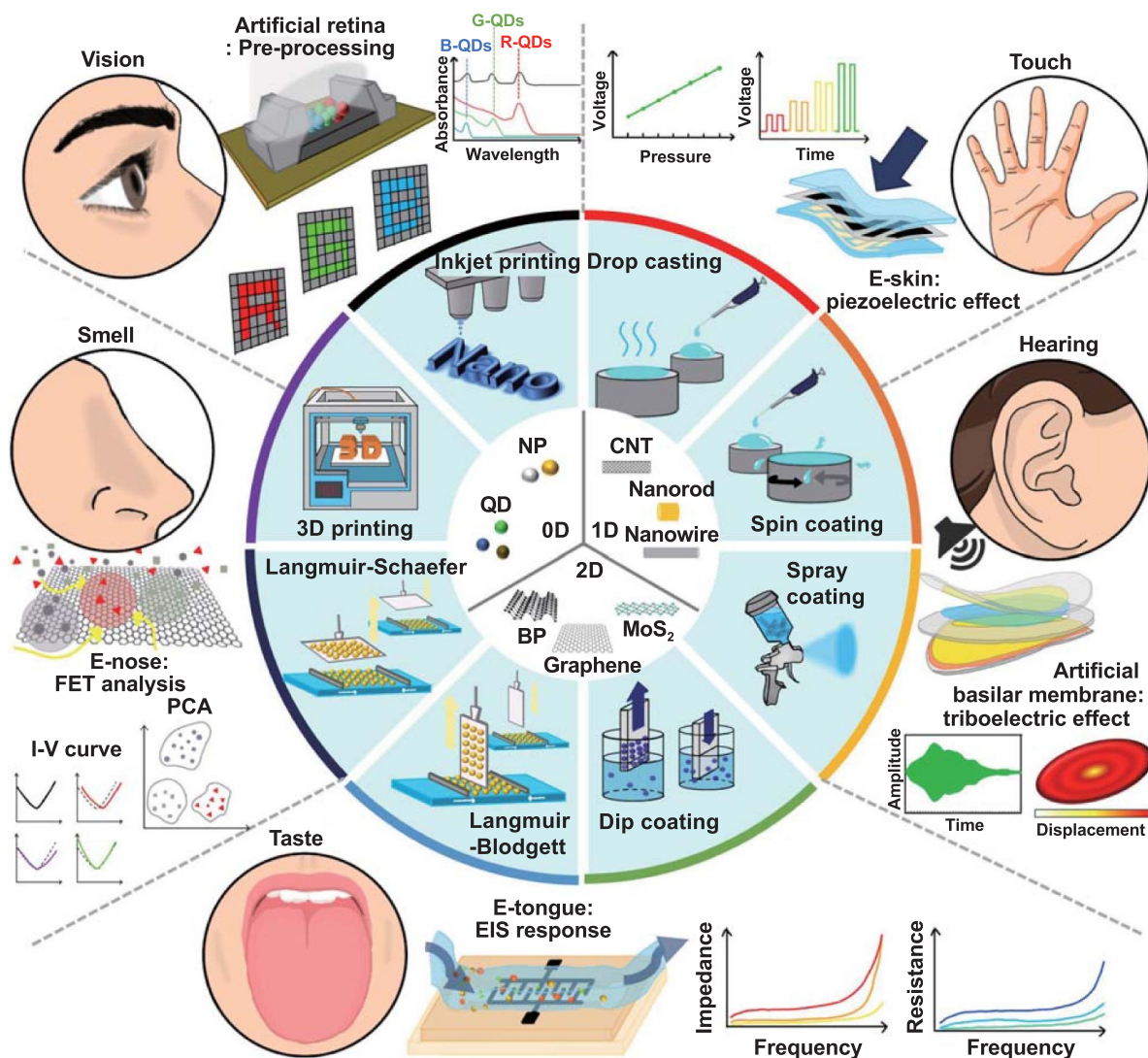


Figure 1. Schematic illustrations of solution-processed nanomaterials for artificial sensory system development. Versatile dimension of nanomaterials including 0D, 1D, and 2D has been integrated with five human senses of artificial sensory devices via evaporation-based assembly (drop casting, spin coating spray coating, and dip coating), assisted assembly (Langmuir–Blodgett, Langmuir–Schaefer), and direct patterning (3D printing and inkjet printing).

2. Solution-processing of low-dimensional nanomaterials

Solution-based processing has been developed in an effort to utilize low-dimensional nanomaterials for coating/printing-based scalable applications for artificial sensory system [27, 32, 34, 36, 37]. This scalable approach mainly consists of bottom-up methods such as precursor-based chemical synthesis/assembly [37, 43–45] and top-down ones, for example, liquid-phase exfoliation, alkali-metal intercalation, and electrochemical exfoliation based on the resulting morphology and characteristics of target materials [32, 46, 47]. A representative example of the bottom-up method is to synthesize 0D halide perovskite from their precursors [43, 44, 48]. Protesescu *et al* reported liquid-phase precursor-based synthesis of 0D all-inorganic cesium-lead halide perovskite, CsPbX_3 ($X = \text{Cl, Br, and I}$), and nanocrystals (NCs) [43]. To enable the synthesis of monodisperse NC colloidal suspensions, the authors revisited

an old-fashioned metal chalcogenide NC synthesis method, namely the hot injection method, where additional Cs precursors were quickly injected (figure 2(a-i)) [49]. Consequently, the resulting CsPbX_3 NC suspensions show continuously tunable photoluminescence (PL) emission with high color purity in the range of visible wavelength based on the ratio of halide elements. The corresponding transmission electron microscope (TEM) image shows that the synthesized CsPbX_3 NCs are nearly monodisperse in size (figure 2(a-ii)) [49]. Another similar example of solution-based approach is to synthesize 0D metallic nanoparticles in liquid-phase [50, 51]. For example, gold nanoparticles (AuNPs) can be synthesized during a chemical reaction of hydrogen tetrachloroaurate(III) trihydrate in an acid. Moreover, morphology and size of AuNPs can be further modulated by utilizing various stabilizers such as polyaniline, lipoic acid, dodecanthiol, and so on. One resulting structure of AuNPs is a hollow sphere of polyaniline/Au composites with an average diameter of 30 nm

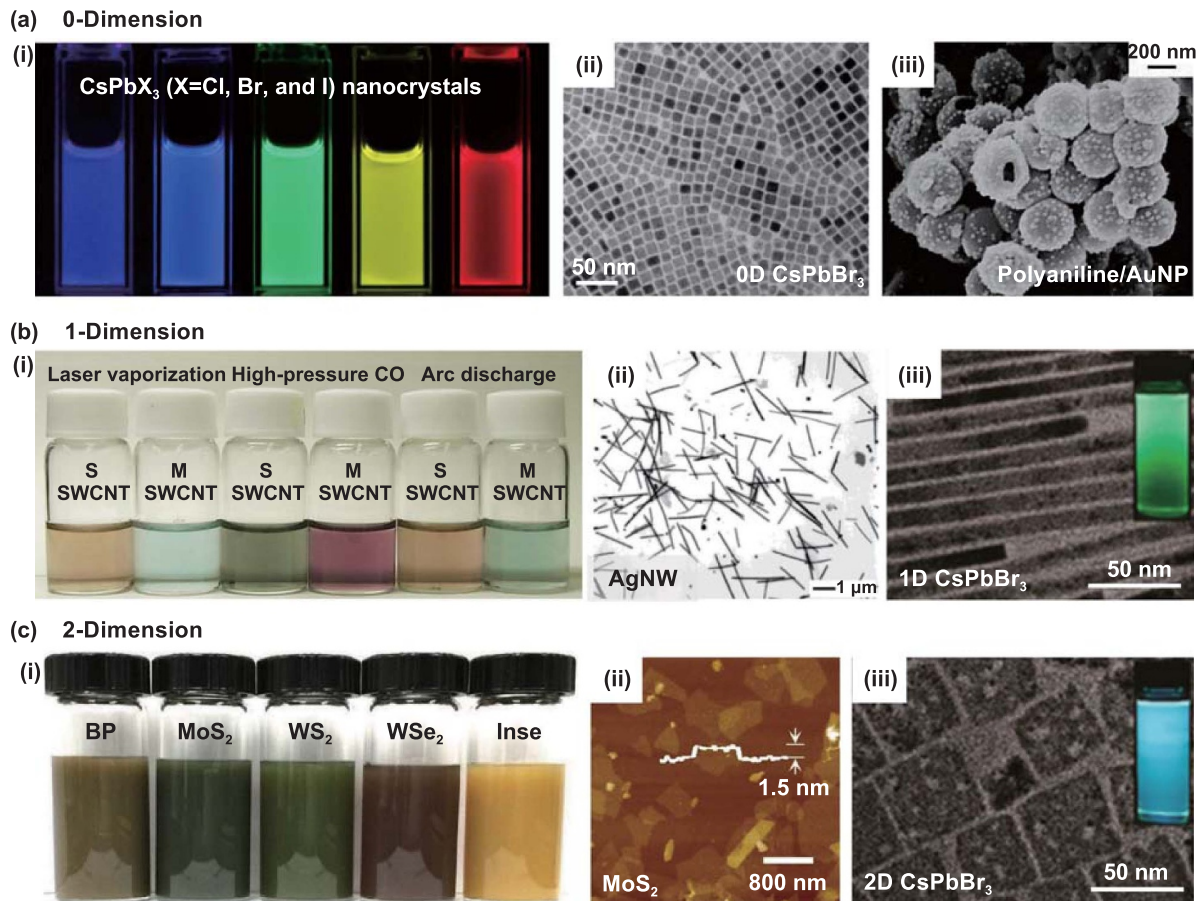


Figure 2. Processable solutions of 0D, 1D, and 2D nanomaterials for artificial sensory system. (a) 0D nanomaterials for artificial sensory system. (a-i) Photograph of the quantum dot (QD) dispersions. Reprinted with permission from [49]. Copyright 2017 American Chemical Society. (a-ii) TEM image of a colloidal dispersion of CsPbBr₃ NCs prepared by precursor-based solution-phase synthesis. Reprinted with permission from [49]. Copyright (2017) American Chemical Society. (a-iii) Scanning electron microscopy (SEM) image of liquid-phase synthesized conducting polymer/noble metal nanoparticle (CP/NMNP). Reprinted with permission from [50]. Copyright (2006) American Chemical Society. (b) 1D nanomaterials for artificial sensory system. (b-i) Photograph of metallic (M) and semiconducting (S) single-wall CNT (SWCNT) dispersions synthesized by LV, HiPCO and Arc. Reprinted from [57], Copyright © 2008 Elsevier B.V. All rights reserved. (b-ii) TEM of as-synthesized AgNW by soft solution-processing. Reprinted with permission from [61]. Copyright (2002) American Chemical Society. (b-iii) TEM of colloidal synthesized ultra-thin CsPbBr₃ NWs. The inset shows the photograph of 1D CsPbBr₃ dispersion. Reprinted with permission from [64]. Copyright (2016) American Chemical Society. (c) 2D nanomaterials for artificial sensory system. (c-i) Photograph of BP, MoS₂, WS₂, WSe₂, and InSe dispersions. [67] John Wiley & Sons. © 2018 WILEY-VCH Verlag GmbH & Co. KGaA, Weinheim. (c-ii) Atomic force microscope (AFM) image of MoS₂ nanosheets produced by electrochemical exfoliation. Reproduced from [70], with permission from Springer Nature. (c-iii) TEM image of CsPbBr₃ nanoplates prepared by self-assembly synthesis. Reprinted with permission from [64]. Copyright (2016) American Chemical Society.

(figure 2(a-iii)) [50]. Although a large quantity of such metallic nanoparticles can be successfully synthesized in solution, their structural inhomogeneity (e.g. spherical, rhombic dodecahedra, and bipyramid) is detrimental to control over their expected optical properties [40, 52, 53]. Therefore, this approach further requires post-processing to purify their structural polydispersity.

Solution-based synthesis of 1D and 2D nanostructures is more challenging than that of 0D due to their high structural anisotropy. Therefore, it is straightforward to exfoliate their 3D structures by applying mechanical force such as ultrasonication, shear mixing, and ball-milling as top-down

approaches [54–56]. As shown in figure 2(b-i) [57], stable dispersions of each semiconducting and metallic (denoted as S and M, respectively) carbon nanotubes (CNTs) can be prepared via liquid-phase exfoliation of CNT bundles synthesized in various ways including laser vaporization, high pressure CO conversion, and arc discharge. Regardless of the type, such CNTs possess a hydrophobic surface. Therefore, it has been highly required to investigate various amphiphilic surfactants (e.g. sodium cholate, sodium dodecylsulfate, Pluronic, and Tetronics) to stabilize CNTs in aqueous solution [57, 58]. Amphiphilic surfactants consist of each hydrophobic and hydrophilic part where a hydrophobic part is wrapping on the

surface of CNTs and a hydrophilic one helps stabilize CNTs in an aqueous medium [58, 59].

Unlike to prepare a stable CNT dispersion, various bottom-up approaches have been introduced to synthesize 1D nanostructures including silver NWs (AgNWs) [60, 61] and halide perovskite NWs [45, 62–65]. AgNWs dispersions can be prepared by a template-directed synthesis with high yield, controllable morphology, and high aspect ratio. For example, platinum nanoparticles are formed by reducing PtCl_2 with ethylene glycol heated to $\sim 160^\circ\text{C}$ (figure 2(b-ii)) [61]. This creates seeds for the heterogeneous nucleation and growth of Ag in the solution. Then, AgNO_3 and poly(vinyl pyrrolidone) are added to the refluxing solution to form AgNWs with an aspect ratio of ~ 1000 and a lateral dimension of ~ 40 nm through the reduction of AgNO_3 by ethylene glycol. 1D perovskite NWs can be easily prepared by solution-phase synthesis, which has the advantages of high crystallinity, large-area, and low-temperature processability [62]. Zhang *et al* synthesized ultrathin single-crystalline CsPbX_3 NWs with a diameter of 2.2 nm by reacting Cs-oleate solutions with lead halide in the presence of oleic acid and oleylamine in octadecene at $\sim 150^\circ\text{C}$. The strong quantum confinement effect contributed to a high PL quantum yield (figure 2(b-iii)) [64, 65].

In a similar manner, 2D nanomaterials also can be synthesized via either top-down and bottom-up approaches in solution. In a straightforward way, various layered crystals can be exfoliated into their 2D nanosheet structure as a top-down approach by applying mechanical shear force and/or electrochemical potential to overcome their weak sheet-to-sheet van der Waals interactions [46, 47]. First, layered crystals can be exfoliated and stabilized in solution via liquid-phase exfoliation methods including ultrasonication, shear mixing, and ball milling [54–56]. The resulting exfoliated 2D nanosheets can be stabilized in various organic solvents, where solvents with high boiling point and desired surface tension (~ 40 mJ m $^{-2}$) are preferred such as *N*-methylpyrrolidone (NMP) and dimethylformamide (DMF). However, 2D dispersions in NMP and DMF are highly restricted to use in solid-state applications due to potential difficulties of complete evaporation of solvents without materials degradation [39]. To address this issue, mixed solvent system with low boiling solvents (e.g. water and alcohol) to match surface tension or stabilizer-assisted aqueous system have been reported [39, 66]. As shown in figure 2(c-i), various 2D semiconductors including BP, MoS_2 , WS_2 , WSe_2 , and InSe are successfully stabilized in a low boiling point deoxygenated ethanol–water cosolvent mixture [67].

Intercalation-based exfoliation methods are another type of solution-based processing for scalable synthesis of 2D nanosheets via van der Waals weakening [34, 68, 69]. An alkali-metal intercalation-based exfoliation has been reported to obtain 2D nanosheets with micrometer-scale lateral size by intercalating alkali ions (e.g. Li, Na, and K) into layered materials [68]. However, the resulting 2D nanosheets suffer from an undesired semiconducting to metallic phase transition due to the insertion of alkali ions and associated electrons. To overcome this limitation, Lin *et al* reported that a molecular intercalation-based exfoliation using relatively large-sized

quaternary alkyl ammonium molecules can reduce electron injection, resulting in the prevention of undesired phase transitions [34]. The resulting nanosheets possess micrometer-scale lateral size, atomically thin and highly monodisperse (figure 2(c-ii)) [70].

Among 2D nanomaterials, graphene oxide (GO) is generally obtained via Hummer's method, which oxidizes graphite by stirring and treating with KMnO_4 and NaNO_3 in concentrated H_2SO_4 [71]. The resulting GO nanosheets can be easily dispersed in various organic solvents, but this procedure involves the generation of toxic gases such as NO_2 or N_2O_4 [72]. To overcome this limitation, compared to Hummer's method, an improved GO production way was introduced that does not involve large exotherm and produce toxic gases. Moreover, the GO dispersions prepared by the improved method had well-oxidized hydrophilic carbon materials and more regular structures [73, 74].

In the meantime, 2D halide perovskites (e.g. Ruddlesden-Popper phase) can be synthesized in solution [75–77]. By synthesizing individual crystals and systematically arranging the connections between them, 2D superlattice NCs can be synthesized [78]. As a strategy to create such 2D structures, layer-by-layer stacking or solvent evaporation-based self-assembly processes are used to create 2D layered structures [79–81]. This solution-processed crystallization creates well-designed nanoscale 2D structured perovskites with high uniformity in shape, size, and chemical composition [82]. For example, Zhang *et al* reported the self-assembly of 2D perovskite nanostructures, a simple approach to fabricate large-scale 2D halide perovskite superlattices with atomic scale precision (figure 2(c-iii)) [64]. PbBr_2 in 1 octadecene is degassed in vacuum, then oleic acid, octanoic acid, and octylamine are injected under N_2 at 150°C to solubilize the PbBr_2 . Following the injection of Cs-oleate and rapid cooling, 2D nanosheets are obtained. Interestingly, the assembled 2D superlattice can be reversibly disassembled back into their building blocks by sonication [65].

By mass-producing nanomaterials as processable solutions through various solution-phase producing techniques, the foundation for forming large-area artificial sensing channels via coating/printing processes has been laid. The synthesized dispersion-based nanomaterials exhibit tailored structural and functional surface properties due to apparent differences in dimensional structures, which can be applied to various sensing platforms [23, 24]. For example, quantum-scale 0D structures with many active edge sites have excellent sensitivity to external stimuli and exhibit high PL properties due to the quantum confinement and edge effects, which can be applied to biosensing and fluorescence-based artificial sensory platforms [23, 83, 84]. 1D nanostructures have high current carrying capacity and stretchability along with structural advantages such as large surface-to-volume ratio and length-to-diameter ratio, which can be advantageously used in artificial strain or environmental sensors [24, 85]. Additionally, 2D nanostructures have atomically-thin thickness, excellent charge carrier mobility, and high on/off ratios with high sensitivity in artificial sensory applications such as photodetection and gas sensing [23, 25, 86].

3. Post-processing for structural purification of low-dimensional nanomaterials

After the dispersion and synthesis of sensor materials in a bulk solution, the purification process should be employed to sort the nanomaterials toward structural monodispersity with specific physical properties because particular structure of low-dimensional nanomaterials is highly correlated to their unique characteristics [23]. For example, 0D AuNPs exhibit distinct optical properties (e.g. localized surface plasmon resonant (LSPR) peaks) based on their shapes [40, 87]. 1D CNTs exhibit either semiconducting or metallic properties based on their chirality. Moreover, semiconducting CNTs can possess various energy bandgaps based on their chiral information [41, 57, 59, 88]. Similarly, 2D nanosheets have thickness-dependent electronic and/or optical properties. For example, 2D semiconducting MoS₂ nanosheets show an indirect-to-direct energy bandgap transition in their atomically thin limit [89–91].

A density gradient ultracentrifugation (DGU) method is typically used to separate nanostructures with desired sensing properties, reducing structural heterogeneity and polydispersity of the bulk solution, and prepares them for the next stage of the printing process applications [91]. Centrifugation-based purification process can be accomplished by two methods: sedimentation-based density gradient ultracentrifugation (s-DGU) [40, 92] and isopycnic density gradient ultracentrifugation (i-DGU) [89, 93]. s-DGU typically utilizes the size-dependent sedimentation rate of nanomaterials, with larger materials settling faster in the presence of centrifugal forces. Additionally, multiple centrifugation steps can be used for subtle separation. i-DGU utilizes a density gradient designed to match the size-dependent buoyant density distribution of nanomaterials. During the process, nanomaterials settle to each isopycnic point. The buoyant density depends strongly on the thickness, providing exceptionally high monodispersity in the thickness of the nanomaterials.

For the purification of 0D nanomaterials, the as-synthesized mixture was centrifuged with a density gradient to separate nanostructures with different diameters and shapes that could not be separated by conventional filtration methods such as a commercial syringe filter [40, 53]. For example, when a highly concentrated synthesized AuNP dispersion (figure 3(a-i)) was loaded into a density gradient medium with a high viscosity, particles with bipyramids structure and rhombic dodecahedra structure were distinguished due to the difference in settling rates depending on particle size (figure 3(a-iii)) [40]. As shown in SEM images of the unsorted mixture (figure 3(a-ii)), bipyramids (figure 3(a-iv)), and rhombic dodecahedra structure (figures 3(a-v)), distinct separation was observed before and after centrifugation. The shape of the AuNP dominates their optical properties such as light absorption and scattering, which in turn affects their LSPR that determines the sensitivity of the optical sensor. Therefore, differences in the dominant dipolar plasmon resonance were also found for the sorted AuNP (figure 3(a-vi)) [40].

SWCNT are typically divided into semiconducting and metallic types, and this distinction is crucial for the performances of sensor devices, requiring the precise purification [41, 42, 58, 88]. The aqueous two-phase (ATP) sorting method is a representative technique that allows for the separate purification of metallic and semiconducting SWCNT (figure 3(b-i)) [94]. Due to differences in properties such as diameter and surface hydrophobicity, the SWCNT mixtures were sorted into two phases, and high-purity semiconducting and metallic SWCNTs were obtained by performing multiple cycles of ATP. Figure 3(b-ii) shows the structures of SWCNTs sorted by diameter via centrifugation and the films formed from them [59]. The sorted SWCNTs exhibited distinct color differences, indicating their different light absorbing bandgap structures. By measuring the optical absorption spectra of the three SWCNT dispersions, differences in peak positions of the absorption band (S_{22}) were observed (figure 3(b-iii)) [41]. The spectra of metallic SWCNTs showed a weak S_{22} peak around 1029 nm, while the peaks of the unsorted mixture and semiconducting SWCNTs appeared at 1000 nm and 980 nm, respectively.

Next, 2D materials also require a separation process to obtain the desired optoelectrical properties. For example, BP dispersions were isolated by s-DGU depending on lateral size when settled in a linear density gradient medium (figure 3(c-i)) [92]. After s-DGU, by analyzing the BP flake area, the homogeneity of the lateral size of BP nanosheets was achieved (figure 3(c-ii)). For i-DGU of 2D nanosheets, dispersions are introduced into a density gradient designed to correspond to the size-specific buoyant density distribution of the desired nanosheets [89, 93]. During ultracentrifugation, 2D nanosheets sediments through the gradient in the centrifuge tube to their isopycnic point. For example, in i-DGU of graphene dispersions, the thickness of flakes controlled by density differentiation and clear visual bands can be observed in centrifuge tubes of graphene dispersions (figure 3(c-iii)) [95]. AFM images and line profiles of graphene flakes from f4 and f16 fractions confirmed that the sorted graphene flakes were monolayer or bilayer with extremely narrow thickness distribution (figure 3(c-iv)). Halide perovskite, another 2D material, can be structurally purified by centrifuging as-synthesized solution. The resulting suspension can be centrifuged at different speeds depending on its size and cleaned to remove the supernatant. The purified 2D halide perovskite solutions showed high uniformity in shape and size [77, 78, 81, 82].

4. Integration of solution-processed nanomaterials with artificial sensory devices

After purifying nanomaterials with the desired functionalities, the next step is to integrate the nanomaterials into the desired device components of the artificial human sensory system. Uniform and stable coating/printing of the processed nanomaterials to specific parts of the device such as channels,

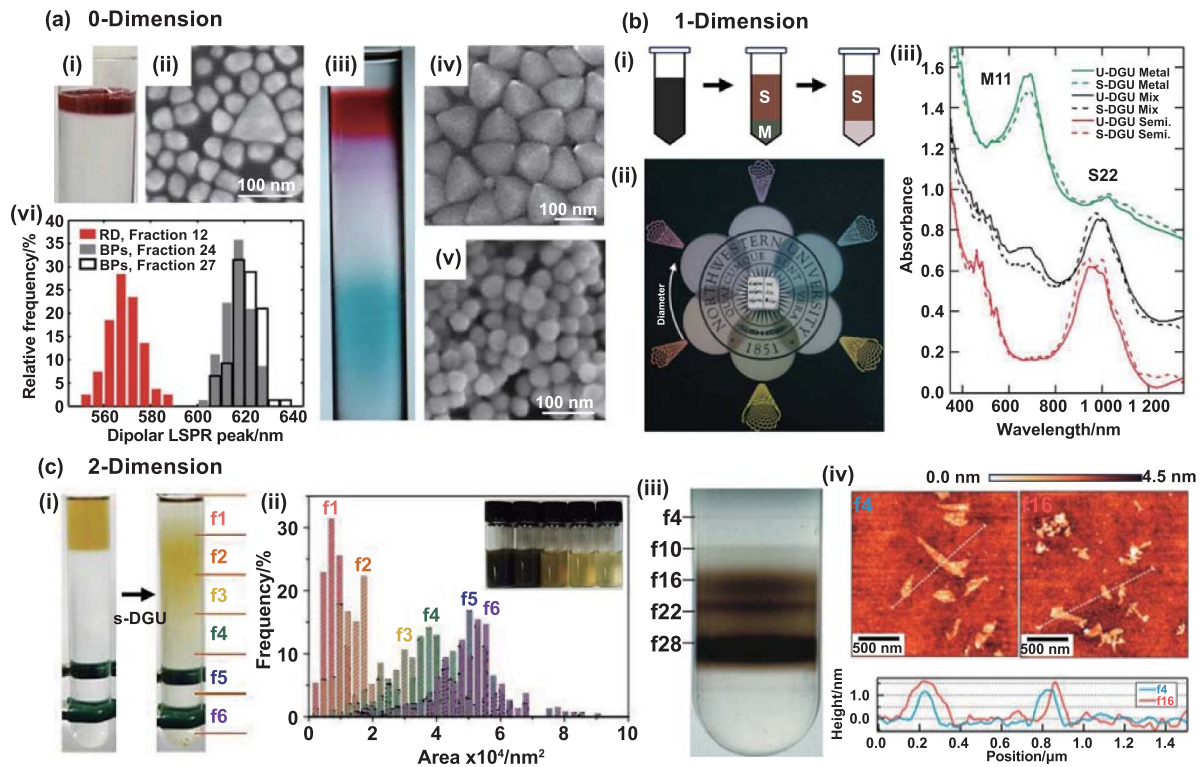


Figure 3. Purification processes of 0D, 1D, and 2D nanomaterials. (a) Purification process of 0D nanomaterials. (a-i) Photograph of a centrifuge tube before centrifugation of AuNP solution. (a-ii) SEM image of unsorted AuNP. (a-iii) Photograph of a centrifuge tube after centrifugation. (a-iv) SEM images of bipyramids structure. (a-v) SEM images of rhombic dodecahedra structure. (a-vi) Distribution of dipolar plasmon resonance in sorted AuNPs. [40] John Wiley & Sons. Copyright © 2013 WILEY-VCH Verlag GmbH & Co. KGaA, Weinheim. (b) Purification process of 1D nanomaterials. (b-i) Schematics of the i-DGU of SWCNTs. (b-ii) Photograph of SWCNT films arranged in order of increasing mean diameter by centrifugation. Reprinted with permission from [59]. Copyright (2008) American Chemical Society. (b-iii) Optical absorption spectra of the metallic, mixed, and semiconducting SWCNTs. Reprinted with permission from [41]. Copyright (2011) American Chemical Society. (c) Purification process of 2D nanomaterials. (c-i) Photograph of few-layer phosphorene (FL-P) solution before and after size sorting. Reproduced with permission from [92]. Copyright (2016) National Academy of Sciences. (c-ii) Histogram of flake areas. The inset shows the photograph of BP dispersions. Reproduced with permission from [92]. Copyright (2016) National Academy of Sciences. (c-iii) Photograph of a centrifuge tube following the first iteration of DGU. Reprinted with permission from [95]. Copyright (2009) American Chemical Society. (c-iv) AFM images of graphene deposited using fractions f4 and f16 (top) and height profile of graphene flakes (bottom). Reprinted with permission from [95]. Copyright (2009) American Chemical Society.

gates, or electrodes is critical for reliable and high performances of the applications. Versatile coating/printing techniques of the solution-processed nanomaterials have been developed to achieve this including (i) evaporation-based technique that induces evaporation of the solution to bind the material to a specific area, (ii) assisted assembly that uses the device surface structure for patterning, and (iii) direct patterning that involves using a nozzle to pattern the solidified material directly onto the desired area (figure 4).

4.1. Evaporation-based assembly of solution-processed nanomaterials

Solution-processed nanomaterials can be directly self-assembled onto sensor devices exploiting three-phase dynamics of evaporating droplet interfaces. First, the drop casting process typically involves placing a large droplet of colloidal nanomaterial onto a target region of the substrates allowing the solvents to evaporate until the film has fully dried. Fox *et al* used the drop casting method of AgNWs through the

contact, spreading, evaporation, and film formation stages (figure 4(a-i)). SEM images show that AgNWs are deposited on substrates based on various concentrations demonstrating that higher concentrations lead to the formation of denser NW networks (figure 4(a-ii)) [96]. Drop casting is regarded as the most basic technique for fabricating nanomaterial films for sensory device configurations, which is widely employed across all dimensions of materials including 0D [97–100], 1D [74, 101], and 2D [102, 103]. Here, the coffee ring effect is usually applied during drop casting, which can result non-uniform deposition pattern where nanomaterials accumulate at the periphery due to the outward flow caused by a specific capillary flow [104]. Spin coating, another typical way of evaporation-based technique, uses a spinning of nanomaterials droplets on the vacuum-fixed substrate on the rotator at high speeds around hundreds of rotations per minute (rpm). Centrifugal force causes the spreading of excess solution, resulting in a thin and uniform coating of the nanomaterials [105]. Jo *et al* fabricated conductive films with dense network junctions by spin coating CNT networks (figure 4(b-i)),

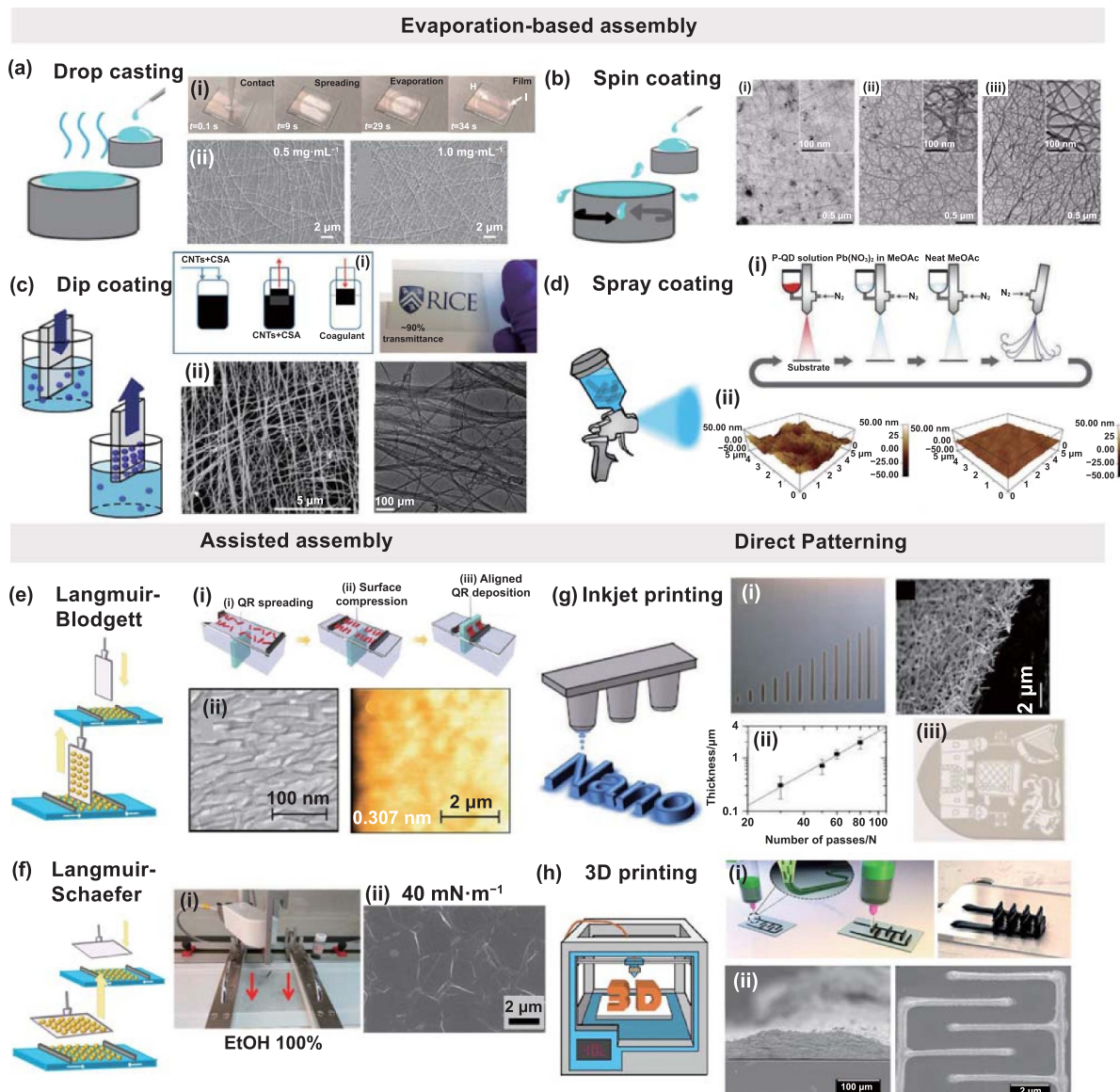


Figure 4. Evaporation-based assembly, assisted assembly, and direct patterning method of solution-processed nanomaterials for sensory device integrations. (a) Drop casting process. (a-i) Drop casting process of AgNWs suspension on superhydrophilic surface. (a-ii) SEM images of the AgNWs network. Reprinted with permission from [96]. Copyright (2021) American Chemical Society. (b) Spin coating process. TEM images of the spin coated SWCNT network of (b-i) the pristine, (b-ii) the cleansed, and (b-iii) HNO₃ and SOCl₂ treated film. Reprinted with permission from [106]. Copyright (2010) American Chemical Society. (c) Dip coating process. (c-i) Schematics of forming a CNT-CSA film on a glass substrate by dip coating. (c-ii) SEM image and (c-iii) TEM image of CNT networks. Reprinted with permission from [110]. Copyright (2012) American Chemical Society. (d) Spray coating process. (d-i) Formation process of CsPbI₃ QD film on a glass substrate via spray coating. (d-ii) AFM images of the QD film surface. [114] John Wiley & Sons. © 2019 WILEY-VCH Verlag GmbH & Co. KGaA, Weinheim. (e) Langmuir-Blodgett process. (e-i) Schematics of LB technique process of transferring QR onto the ZnO sol-gel/ITO substrate. (e-ii) SEM image and AFM image of the QR film. [122] John Wiley & Sons. © 2021 Wiley-VCH GmbH. (f) Langmuir-Schaefer process. (f-i) Photograph of spreading MXene nanosheets on a silicon substrate by LS technique. (f-ii) SEM image of MXene. Reprinted with permission from [128]. Copyright (2020) American Chemical Society. (g) Inkjet printing process. (g-i) Different lengths of printed AgNWs on a PET substrate by inkjet printing and SEM image of the edge. (g-ii) Network thickness as a function of the number of passes. (g-iii) AgNWs network in the complex shape. Reprinted with permission from [137]. Copyright (2015) American Chemical Society. (h) 3D printing process. (h-i) Schematics and photograph of the 3D printing of MSCs on hydrophilic substrate. (h-ii) SEM images of the electrode in the MSC device. Reprinted with permission from [147]. Copyright (2019) American Chemical Society.

which were further processed through washing (figure 4(b-ii)) and treated with HNO₃ and SOCl₂ (figure 4(b-iii)) [106]. This method allows for rapid and uniform coverage over large areas within just a few seconds to minutes, but it leads to a significant loss of nanomaterial solutions during coating [107, 108].

It also faces challenges in achieving uniform coatings on non-planar substrates. Dip coating, on the contrary, involves the immersing process of the target substrate into a colloidal dispersion, where nanomaterials adhere to target surfaces [109]. This adhesion continues as the substrate is withdrawn from the

liquid, leading to the formation of a coherent film that solidifies through drying and subsequent chemical reactions. Mirri *et al* immersed the glass slide into the CNT-chlorosulfonic acid (CSA) solution and withdrew at a controlled speed to make a transparent film (figure 4(c-i)). The film comprises well-aligned CNT bundles corresponding to the coating direction and ensures isotropic film conductivity (figure 4(c-ii)) [110]. The dip coating process is often executed with a controlling withdrawal speed to get monodisperse NC films [111]. Spray coating is another widely used technique for making relatively large-area nanomaterials film up to a meter scale compared to previous methods [112], where the fine droplets of colloidal particles are sprayed onto temperature-controlled substrates. Temperatures are set ranging from low to high depending on the type of nanomaterial and the characteristics of the substrate and evaporation following the spraying of particles mediates the film formation [113]. Yuan *et al* spray coated the colloidal inorganic perovskite CsPbI₃ QDs in a fully automated manner for the ultrathin-film purification (UFP) formation (figure 4(d-i)). Figure 4(d-ii) shows samples where UFP technology has been applied demonstrating significantly smoother film formation with a root-mean-square roughness of 1.38 nm when measured via AFM (left, figure 4(d-ii)), compared to directly spray coated samples that exhibit a roughness of 6.60 nm (right, figure 4(d-ii)) [114]. Moreover, a distinctive advantage of spray coating is that it can be easily applied on 3D complex substrates such as semiconducting chips [115] and surgical masks [116] without being constrained by the type of printing nanomaterials [117–120].

4.2. Assisted assembly of solution-processed nanomaterials

Assisted assembly methods leverage the material features such as the size and polarity of the particles with the assistance of target substrate characteristics [121]. There are two representative assisted assembly methods: LB and LS coating. The LB method disperses nanomaterials in volatile organic carriers on an aqueous subphase. The materials are compressed into a densely packed monolayer by systematically reducing the surface area with dual mechanical barriers. Rhee *et al* utilized the LB method to fabricate films of quantum nanorods (QRs), colloquially known as ‘dot-in-rod’, distinguished by their unique structural characteristic of rod-shaped shells encasing spherical QDs (figure 4(e-i)). This approach entails the methodical adjustment of the substrate position for the successive stacking of monolayer films, aiming to construct a film with multiple layers. This process effectively demonstrates the adaptability of the printing technique in fabricating complex layered structures. Figure 4(e-ii) demonstrates that the LB deposited QR film exhibits unidirectional orientation and creates a thin film with uniform thickness [122]. LB method has been utilized to achieve high coverage of nanoparticles [123], nanosheets [124], and a concurrent alignment of NWs [125] or CNTs [126] on the substrate. Compared to the LB method, the LS method relies on horizontal movements of target substrates. This involves either stamping the substrate onto the water phase surface from above or lifting the substrate immersed in the water phase, thus forming a monolayer

by considering the hydrophilic and hydrophobic properties of nanomaterials. This horizontal transfer is particularly advantageous for certain types of films, offering a more controlled and uniform monolayer deposition, especially for materials with complex or sensitive surface properties [127]. Kim *et al* used LS methods to create a large area film of MXene monolayers (figure 4(f-i)). The MXene platelets are completely covered, leaving nearly no gaps between them when the surface pressure (π) reaches 40 mN·m⁻¹ (figure 4(f-ii)) [128]. The LB technique facilitates the flawless formation of monolayers from solution-based nanomaterials, while the LS technique extends this capability to create thicker multilayered films [129–131]. However, both LB and LS techniques require the careful maintenance of stable nanomaterial dispersions within an aqueous subphase, and the need for precise control over sensitive processing conditions presents limitations in terms of scalability [132].

4.3. Direct patterning of solution-processed nanomaterials

While the evaporation-based and assisted assembly can create uniform thin films of nanomaterials on larger planar substrates, it is crucial to achieve few micrometers precision of patterning onto pre-determined sensor device areas. There is an increasing focus on developing inks from colloidal nanomaterials and using 3D printers to directly form patterns on target surfaces [133–135]. Inkjet and 3D printing technologies are becoming more popular because they allow for the flexible creation of various structures using nanomaterials. Inkjet printing can use very small volumes of fluid, typically less than 100 pico-liters for nanomaterials dispensing. Thus, understanding how the physical processes that occur during inkjet printing interact with the properties of the fluid precursors used is crucial for achieving functional objectives [136]. Finn *et al* used inkjet printing to fabricate AgNW pattern structures with length and width controllability and formed a dense network of AgNW with 80 passes (figure 4(g-i)). The number of nozzle passes is linearly proportional to the film thickness (figure 4(g-ii)), enabling rapid production of complicated images (figure 4(g-iii)) [137]. Many researches have recently focused on inkjet printing with high solid content inks, balancing the need for proper viscosity (1 cP ~ 100 cP) for stable nanomaterial mechanisms [138], while also exploring higher viscosity inks and expanding the nanomaterial ink library [139–141]. While inkjet printing is focused on creating 2D planar films, 3D printing has the advantage of incorporating the z-axis for 3D structures [142]. This benefit facilitates the precise deployment of nanomaterials at desired locations through a three-axis system across biological and mechanical systems [143–145], as well as in the patterning for optoelectronic device fabrication [146]. Orangi *et al* used an extrusion method-based 3D printing technique to fabricate the all-solid-state micro-supercapacitors (MSCs) with additive-free and water-based MXene ink. MXene ink was transferred into syringes fitted with nozzles (internal diameters ranging from 230 μ m to 600 μ m). The rheological characteristics of the MXene ink ensured that the extruded layers were structurally strong, allowing the stacking of multiple layers to

construct printed electrodes of several millimeters in height without structural failure (figure 4(h-i)). The printed ink was well aligned horizontally, and patterning occurred as predetermined, confirming the desired configuration (figure 4(h-ii)) [147]. 3D printing of nanomaterial dispersions requires the sensitive selection of appropriate nanomaterials based on the objective and the determination of printing techniques according to the type of nanomaterials [148–150].

5. Design and performance of artificial sensory systems with solution-processed nanomaterials

The human vision system transmits light signals from the retina to the brain through the optic nerve, where synapses strengthened by neuron interactions remember the stimulus information (figure 5(a-i)) [151]. To mimic this, versatile solution-processed nanomaterials including QD, TMDC, CNT, and halide perovskites have been used to fabricate the sensitive photo-absorbing films [152]. Park *et al* fabricated sensitive photo-absorbing films with memorization capabilities to fabricate the artificial eyes using spin coating of QD [151]. By controlling the duration and spike number of light pulses, the photocurrent increased from 0.07 μA to 30.08 μA as the pulse duration increased from 0.05 s to 10 s (figure 5(a-ii)). During repeated irradiation by increasing the number of light pulses up to 200, the photocurrent increased to 32.69 μA (figure 5(a-iii)). These behaviors, along with increased photocurrent accumulation, improved the level of memory retention. To implement a color-recognizable visual system, a 7×7 pixelated photonic synapse array was fabricated. Color image recognition in RGB non-volatile mode from a three-color pattern input led to the identification of specific character images mirrored in each color (figure 5(a-iv)) [151]. As such, the approach to artificial vision system composed of light-absorbing films of versatile low-dimensional materials will be a new way to build artificial color recognition or smart intelligent vision systems such as R/G/B image sensing chips or neuromorphic imaging device [152, 153].

In human olfactory system, odorant molecules interact with specific odorant receptors on olfactory sensory neurons within the upper nasal epithelium, initiating signal transduction to the brain olfactory centers. Mirroring this biological mechanism, the electronic nose (E-nose) concept has been developed. These devices, equipped with multiple sensor arrays comprising electrical transducers, facilitate data acquisition, while the integration of big data analytics enables precise odor identification [154]. Hu *et al* employed a micro-syringe-based drop casting technique to deposit reduced GO (rGO) onto Ag electrodes, constructing a gas sensor capable of detecting ammonia concentrations as low as one parts per billion at room temperature [155]. This technology has been applied to develop a metal-ion-induced-GO-based E-nose, proposed as a non-invasive tool for lung cancer diagnosis through exhaled breath analysis. Chen *et al* fabricated a flexible GO gas sensor array patterned with eight interdigitated electrodes (IDEs) using a simple drop casting method

(figure 5(b-i)). Subsequently, the response of the sensor array to four types of disease-related gases (e.g. acetone, isoprene, ammonia, hydrothion) was analyzed by measuring the current in each of the IDEs. The measured current of the array was then converted into a relative response and subjected to principal component analysis to discriminate between the individual gases. The eight sensing elements in the array exhibited enhanced sensitivity to concentrations of 50 parts per million (ppm) of the tested gases (figure 5(b-ii)). Finally, the clinical EB analysis of both a healthy control group and a lung cancer group was conducted using an artificial neural network (ANN). The results demonstrated a 95.8% sensitivity and 96.0% specificity for the testing set, achieved by randomly assigning 50% of the cases for the training set. Receiver operating characteristic (ROC) curve analysis for the ANN model indicated that the area under the curve (AUC) was 0.996, showcasing a high classification ability (figure 5(b-iii)) [156]. Jin *et al* fabricated an E-nose system by drop casting MoS₂ QD on the Au IDEs to sense various volatile organic compounds (VOCs). The E-nose successfully discriminated 100 ppm levels of acetaldehyde [157]. Lorwongtragool *et al* created a wearable E-nose by inkjet printing of CNTs on polyethylene naphthalate substrate demonstrating its ability to distinguish VOCs from armpit regions in a compact armband format with wireless connectivity [158]. E-noses have advanced as multi-array gas sensors through the integration of diverse nanomaterials [159]. With their broad applicability, E-noses show promise for deployment in environmental quality monitoring to assess atmospheric chemicals and identify toxic and explosive gases [160, 161]. Additionally, they show a potential for significant contributions to clinical healthcare through early diagnosis of exhaled breath from human [162].

Biomimetic taste sensors, inspired by the physicochemical interactions of food molecules with taste receptor cells [163], have evolved into fluid sensors known as electronic tongues (E-tongues). Current designs incorporate a cellular architecture, utilizing an array of taste receptor-specific biological cell lines affixed to electrodes, to emulate biochemical reactions for enhanced sensitivity and specificity [164–166]. Integration with non-biological receptor materials further enhances the capabilities of these biomimetic chemical sensors. Nanomaterial-based E-tongues are mainly fabricated in the form of microfluidic devices. Wagh *et al* employed laser-induced graphene patterning with microfluidic channel integration to fabricate the E-tongue system. They analyzed solutions representing the five basic human tastes using electrochemical impedance spectroscopy, differentiating solution types and concentrations ranging from 1 to 1000 ppm [6]. Facure *et al* developed an E-tongue by drop casting MoS₂ and GO onto Au IDEs. By measuring impedance variations, they distinguished four types of antibiotics at the nanomolar level [167]. Jung *et al* developed a taste bud-inspired, multi-taste sensing device by using various types of nanomaterials and assembly methods for detecting four distinct tastes in a single drop of dietary compounds such as saltiness, sourness, astringency, and sweetness (figure 6(a-i)). The substrate layer was prepared by spin coating polymethyl methacrylate

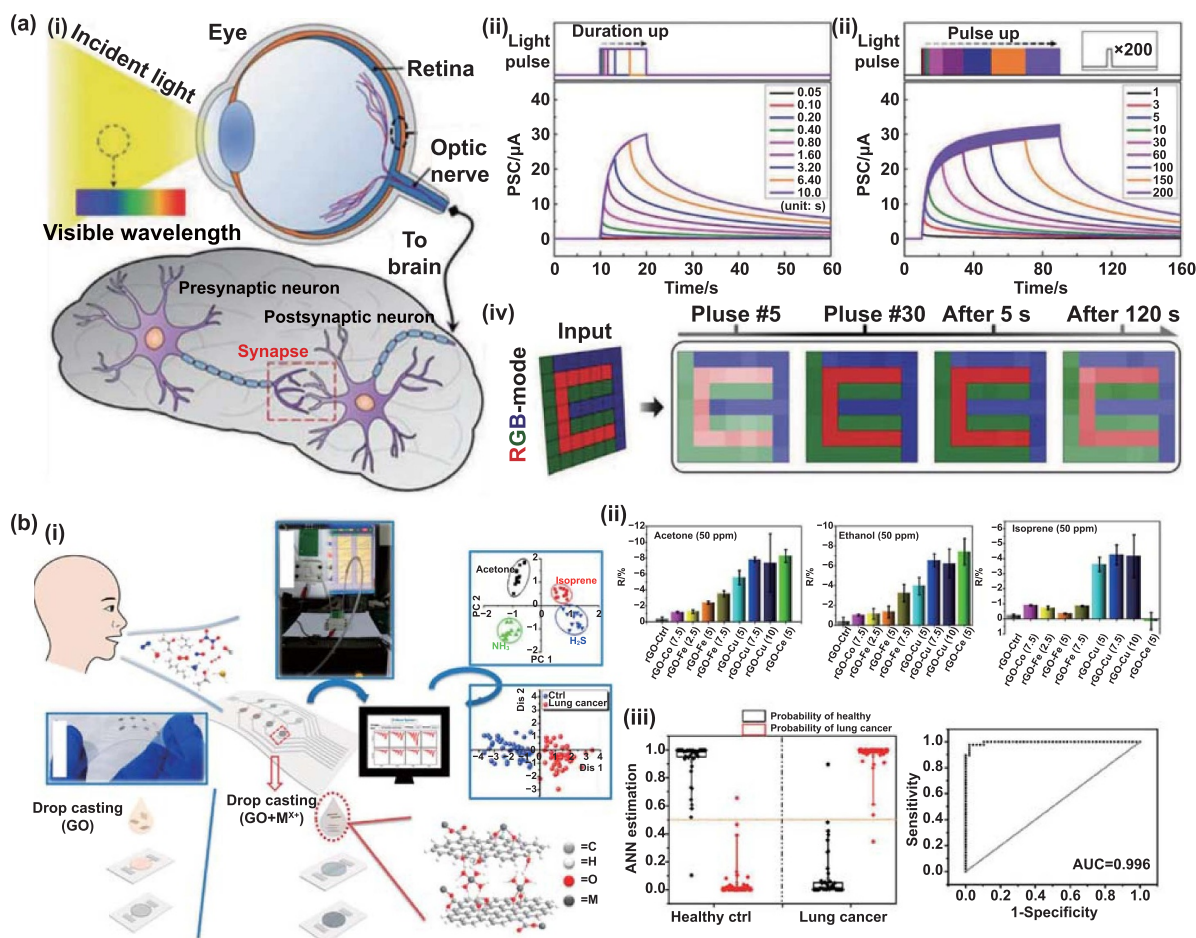


Figure 5. Artificial human eyes and nose devices based on the printing of solution-processed nanomaterials. (a) Artificial human eyes devices. (a-i) Schematics of the human visual recognition system. (a-ii) Pulse duration-dependent photocurrent of artificial photonic synapse system by spin coating of mixed QDs. (a-iii) Pulse number-dependent photocurrent of the device. (a-iv) Contour mapping of the photocurrent measured on each pixel of the array in RGB. [151] John Wiley & Sons. © 2022 Wiley-VCH GmbH. (b) Artificial human nose devices. (b-i) Schematics of E-nose by metal-ion-induced assembly of rGO. (b-ii) Responses of rGO multi-arrays to VOCs. (b-iii) ANN estimation of clinical EB analysis and ROC curve analysis for the ANN model using the E-nose system. Reprinted with permission from [156]. Copyright (2020) American Chemical Society.

(PMMA) onto a Si wafer and the Ti/SiO_2 layer was deposited via drop casting for electrode modifications (figure 6(a-ii)). Four distinct lipid membranes, specifically engineered to detect saltiness, sourness, astringency, and sweetness to mimic natural taste sensing mechanism of human taste buds, were applied onto their respective working electrodes via drop casting (figure 6(a-iii)). To evaluate the analytical performance of each lipid membrane, responses to KCl (saltiness), tartaric acid (sourness), tannic acid (astringency), and sucrose (sweetness) were elicited at various concentrations, measuring the open-circuit potential. The calibration curves for each sensor-taste interaction demonstrated a logarithmic proportionality with the concentration of the respective taste solution (figure 6(a-iv)). Figure 6(a-v) highlighted the high selectivity of membranes in responding to their respective taste stimuli, indicating effective taste discrimination [168]. Drawing on its gustatory origins, the E-tongue specializes in detecting substances in fluids, making it particularly suited for the quality management of food [169], where it is already finding applications in the industry [170]. Mirroring this, its development is

also making strides in the biopharmaceutical sector, especially in the evaluation of oral pharmaceuticals [171].

Human auditory inspired sensors have advanced by mimicking the eardrum detection of vibrational energies and the cochlea conversion of these vibrations into electrical impulses [172]. This process, essentially transforming mechanical pressure into electrical signals, capitalizes on the principles of piezoelectricity [173, 174]. There has been significant progress in the development of implantable artificial auditory devices for practical applications [175–177]. To address the shortcomings associated with the surgical procedure of cochlear implants [178], such as the inconvenience of external devices, high power consumption, and substantial cost [179, 180], recent researches have devised ABMs using Au nanofilms formed via a sputtering system [7, 181, 182]. Gong *et al* introduced an innovative approach for the fabrication of an ABM by inducing point cracks in a distinctive vertically aligned AuNW film (figure 6(b-i)). This was achieved through a dip coating process, where a PMMA coated silicon wafer was submerged in an aqueous solution containing Au

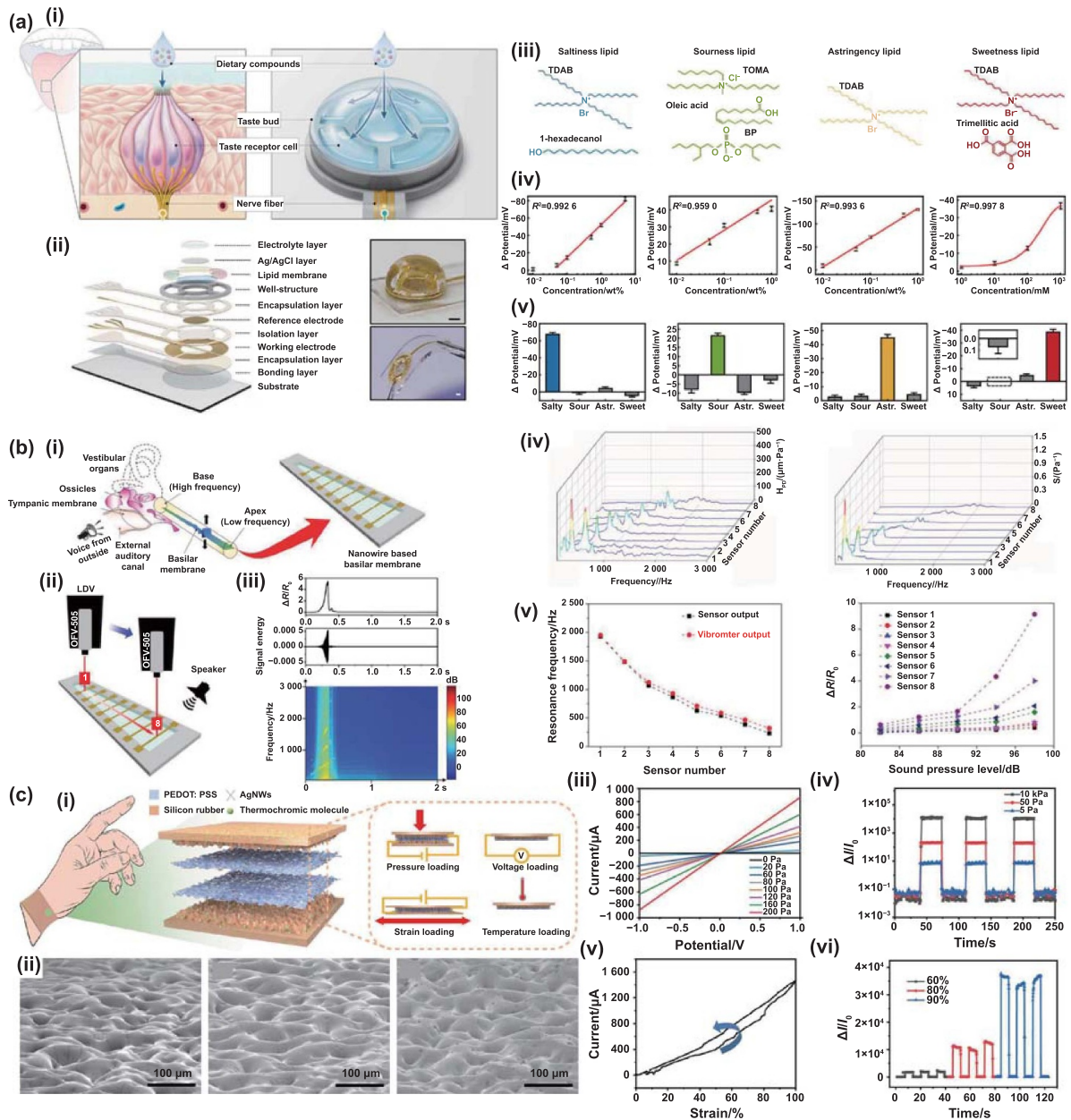


Figure 6. Artificial human tongue, ear, and finger devices based on printing of solution-processed nanomaterials. (a) Artificial human tongue devices. Schematics of (a-i) operating mechanism and (a-ii) device configuration of E-tongue. (a-iii) Four unique lipids corresponding to each of the four distinct tastes. (a-iv) Open-circuit voltage responses of the E-tongue to four tastes. (a-v) Selectivity of lipid membranes for corresponding taste. Reprinted with permission from [168]. Copyright (2023) American Chemical Society. (b) Artificial human ear devices. (b-i) Schematics of human ear with cochlea and dip coated NW-based ABM. (b-ii) Schematics of the printing setup. (b-iii) Sensor resistance response, waveform, and STFT signals to a chirp signal. (b-iv) Acoustic-to-mechanical transfer function and sensitivity for all sensor strips. (b-v) Resonance frequencies of the ABM and sensor output dependency on sound pressure level. [183] John Wiley & Sons. © 2020 WILEY-VCH Verlag GmbH & Co. KGaA, Weinheim. (c) Artificial human finger devices. (c-i) Schematics of structure and sensing modes of E-skin. (c-ii) SEM images of E-skin surface at various stages of fabrication. (c-iii) The I-V curves of the pressure sensor. (c-iv) Pressure sensing during loading/unloading cycles under different applied pressures. (c-v) Hysteresis curves of the strain sensor. (c-vi) Strain sensing during repeated stretching and releasing cycles under varying degrees of applied strain. Reprinted with permission from [188]. Copyright (2021) American Chemical Society.

seeds for a designated duration, facilitating the vertical alignment of AuNWs. To evaluate the performance of this device, acoustic responses from sensor strips were meticulously recorded, employing chirp sounds spanning 40 Hz – 3000 Hz (figure 6(b-ii)). Typical resistance fluctuations, waveform

transformations, and short-time Fourier transform (STFT) signals revealed a significant resonant peak at 575 Hz, signifying the resonance of the first harmonic mode (figure 6(b-iii)). Within the 40 Hz – 3000 Hz range, each sensor strip of the artificial auditory device demonstrated selectivity and sensitivity

to frequency bands corresponding to their lengths, as evidenced by measurements of the acoustic-to-mechanical energy transfer function (figure 6(b-iv)). The consistency between electrical and vibrometer outputs confirmed the precision of resonance frequency measurements. Furthermore, employing custom pure tone stimuli and modifying sound pressure levels demonstrated the suitable dynamic range of the electrical output of the devices (figure 6(b-v)) [183]. Modeled on the human eardrum's intricate structure, the ABM is extensively researched for its potential in clinical implant (CI) [184], with significant studies tailored to animal models to validate its efficacy [185]. Beyond its biological implications, ABM's utility extends to robotics, showcasing its versatility and broad applicability in both medical and technological domains [7].

Tactile sensation is mediated by specialized receptors: thermoreceptors for temperature, nociceptors for pain, and mechanoreceptors for pressure and tactile stimuli. Extending beyond the tactile scope, photoreceptors and chemoreceptors detect light and chemical stimuli, respectively [186]. Owing to these features, artificial electronic-skin (E-skin) inspired by human skin has advanced towards inherently flexible and stretchable structures, evolving to detect temperature, pressure, or both [14, 187]. Xu *et al* designed the stretchable multimode E-skin by spray coating of AgNWs on the colorimetric Si rubber substrate (figure 6(c-i)). Remarkably, this stretchable device retains its ability to accurately sense pressure, strain, temperature, and voltage across four distinct modes even with its inherent stretchability. Furthermore, it demonstrates visual responses, transitioning in color from brown to green, and ultimately to bright yellow. To mimic the surface of human epidermis, the abrasive paper was employed as a template. SEM images show the morphology of a micro patterned Si rubber substrate on abrasive paper, the incorporation of thermochromic molecules, and AgNWs spray coated onto the surface (figure 6(c-ii)). Upon applying different pressures to the fabricated sensor, the current–voltage (I – V) curves were measured, revealing that the slope of these curves was proportional to the pressure (figure 6(c-iii)) and the electrical response during repeated loading/unloading cycles demonstrated excellent accuracy and reliability (figure 6(c-iv)). The performance of the strain sensor was also evaluated, indicating reversible properties through hysteresis curves that represent electrical resistance under applied strain (figure 6(c-v)). The compressive strain sensor exhibited stable and distinguishable responses with excellent repeatability to different compressive strains of 60%, 80%, and 90% (figure 6(c-vi)) [188]. Takei *et al* fabricated a robust and reliable E-skin by parallel printing semiconductor NWs via a stamping technique based on evaporation assembly [189]. Zhang *et al* designed an E-skin by fabricating a stretchable conductor through the patterning of Ag nanoink [190]. As such, E-skin has made considerable progress in materials development and device integration for mechanically bendable and stretchable optoelectronics, broadening its application to soft robotics and internet-of-things devices [191].

6. Summary and outlook

Wide library of dimensions, materials, and printing techniques has been successfully employed in five artificial sensory mimicry systems: vision, olfaction, gustation, audition, and tactile perception. Given the need for sensitivity and integration with large-area devices in artificial sensory systems, nanomaterials must be combined with solution-processing and printing techniques. We have reviewed comprehensive process techniques highlighting specific critical factors at each stage from dispersion-purification to printing-assembly stages.

However, many challenging issues still remain with the use of solution-processed nanomaterials for real-world artificial sensory system applications. First, ambient stability of the materials is essential. During the exfoliation and dispersion processes, nanomaterials may expose surface defects and rich functional groups [192–194]. While ambient oxidation is relatively less significant in liquid dispersion, once they are printed onto actual devices, the nanomaterials become directly exposed to moisture and oxygen, making them prone to performance alterations [195]. Thus, the artificial sensory devices should maintain stable properties under the dynamic ambient conditions of moisture, oxygen, and temperature they will encounter in real-world [196, 197]. Second, research should focus on optimizing the printing process to minimize device-to-device variation [198, 199]. Assisted assembly and 3D printing, which predominantly utilize automated machinery, generally exhibit low device-to-device variation. However, evaporation-based assembly faces challenges in ensuring consistent performance across various environments due to differing evaporation conditions [200]. Detailed optimization of evaporation and coating processes is necessary to ensure users can consistently rely on the same performance from each artificial sensory device [201]. Third, integration with AI-based machine learning software is essential [202–205]. To precisely input the subtle range of stimulations handled by human senses, accurate differentiation between signal and noise is necessary along with essential tasks including abnormal detection and classification of multivariate data [203, 206, 207]. In addition to hardware development that includes materials and devices, there must be the development of high-performance software tailored to complement it [208]. Finally, system integration technology is crucial. It is not only the printing and assembly of materials and devices that must be precisely integrated, but also the systems for data collection and user monitoring. The design rules must be optimized for the size, shape, and mechanical deformations of systems that are tailored to specific sensations. Solution-processed nanomaterials have already achieved significantly high-performance artificial sensory devices. If research in this field is more focused on these remaining challenges using the state-of-the-art solution-processing technologies reviewed in this paper, we can truly enter an era of big digital transformation, where it becomes feasible to transport the sensory information of all live beings on the earth into the virtual world.

Acknowledgments

This research was supported by the National Research Foundation (NRF) grant funded by the Korean government (MSIT) (No. RS-2023-00237308).

ORCID iDs

Okin Song  <https://orcid.org/0009-0003-6800-5131>
 Youngwook Cho  <https://orcid.org/0009-0006-4403-3519>
 Soo-Yeon Cho  <https://orcid.org/0000-0001-6294-1154>
 Joohoon Kang  <https://orcid.org/0000-0002-6578-2547>

References

- [1] Wang J W, Wang C, Cai P Q, Luo Y F, Cui Z Q, Loh X J and Chen X D 2021 Artificial sense technology: emulating and extending biological senses *ACS Nano* **15** 18671–8
- [2] Lee Y, Park J, Choe A, Cho S, Kim J and Ko H 2020 Mimicking human and biological skins for multifunctional skin electronics *Adv. Funct. Mater.* **30** 1904523
- [3] Chun S *et al* 2021 An artificial neural tactile sensing system *Nat. Electron.* **4** 429–38
- [4] He Z H, Ye D K, Liu L Y, Di C-A and Zhu D B 2022 Advances in materials and devices for mimicking sensory adaptation *Mater. Horiz.* **9** 147–63
- [5] Hayasaka T, Lin A, Copa V C, Lopez L P Jr, Loberternos R A, Ballesteros L I M, Kubota Y, Liu Y M, Salvador A A and Lin L W 2020 An electronic nose using a single graphene FET and machine learning for water, methanol, and ethanol *Microsyst. Nanoeng.* **6** 50
- [6] Wagh M D, Sahoo S K and Goel S 2022 Laser-induced graphene ablated polymeric microfluidic device with interdigital electrodes for taste sensing application *Sens. Actuators A* **333** 113301
- [7] Guo H Y *et al* 2018 A highly sensitive, self-powered triboelectric auditory sensor for social robotics and hearing aids *Sci. Robot.* **3** eaat2516
- [8] Kim H J and Kim Y J 2018 High performance flexible piezoelectric pressure sensor based on CNTs-doped 0–3 ceramic-epoxy nanocomposites *Mater. Des.* **151** 133–40
- [9] De Paola A, La Cascia M, Lo Re G, Morana M and Ortolani M 2013 Mimicking biological mechanisms for sensory information fusion *Biol. Inspired Cogn. Archit.* **3** 27–38
- [10] Kim Y *et al* 2018 A bioinspired flexible organic artificial afferent nerve *Science* **360** 998–1003
- [11] Wang M *et al* 2020 Gesture recognition using a bioinspired learning architecture that integrates visual data with somatosensory data from stretchable sensors *Nat. Electron.* **3** 563–70
- [12] Wan C J, Cai P, Guo X, Wang M, Matsuhisa N, Yang L, Lv Z, Luo Y, Loh X J and Chen X 2020 An artificial sensory neuron with visual-haptic fusion *Nat. Commun.* **11** 4602
- [13] Wang T, Wang M, Yang L, Li Z Y, Loh X J and Chen X D 2020 Cyber–physiochemical interfaces *Adv. Mater.* **32** 1905522
- [14] Wang M, Luo Y F, Wang T, Wan C J, Pan L, Pan S W, He K, Neo A and Chen X D 2021 Artificial skin perception *Adv. Mater.* **33** 2003014
- [15] Cai P Q, Leow W R, Wang X Y, Wu Y-L and Chen X D 2017 Programmable nano–bio interfaces for functional biointegrated devices *Adv. Mater.* **29** 1605529
- [16] Broza Y Y, Zhou X, Yuan M M, Qu D Y, Zheng Y B, Vishinkin R, Khatib M, Wu W W and Haick H 2019 Disease detection with molecular biomarkers: from chemistry of body fluids to nature-inspired chemical sensors *Chem. Rev.* **119** 11761–817
- [17] Cho S-Y *et al* 2021 Cellular lensing and near infrared fluorescent nanosensor arrays to enable chemical efflux cytometry *Nat. Commun.* **12** 3079
- [18] Gu L L *et al* 2020 A biomimetic eye with a hemispherical perovskite nanowire array retina *Nature* **581** 278–82
- [19] Cai P Q *et al* 2020 Locally coupled electromechanical interfaces based on cytoadhesion-inspired hybrids to identify muscular excitation-contraction signatures *Nat. Commun.* **11** 2183
- [20] Li W L *et al* 2021 An on-demand plant-based actuator created using conformable electrodes *Nat. Electron.* **4** 134–42
- [21] Luo Y F, Li W L, Lin Q Y, Zhang F L, He K, Yang D P, Loh X J and Chen X D 2021 A morphable ionic electrode based on thermogel for non-invasive hairy plant electrophysiology *Adv. Mater.* **33** 2007848
- [22] Heo J H *et al* 2023 Sensor design strategy for environmental and biological monitoring *EcoMat* **5** e12332
- [23] Zhou T T and Zhang T 2021 Recent progress of nanostructured sensing materials from 0D to 3D: overview of structure–property–application relationship for gas sensors *Small Methods* **5** 2100515
- [24] Wang F, Liu S, Shu L and Tao X-M 2017 Low-dimensional carbon based sensors and sensing network for wearable health and environmental monitoring *Carbon* **121** 353–67
- [25] Li B L, Wang J P, Zou H L, Garaj S, Lim C T, Xie J P, Li N B and Leong D T 2016 Low-dimensional transition metal dichalcogenide nanostructures based sensors *Adv. Funct. Mater.* **26** 7034–56
- [26] Yoon M, Lee Y, Lee S, Cho Y, Koh D, Shin S, Tian C, Song Y, Kang J and Cho S-Y 2024 A nIR fluorescent single walled carbon nanotube sensor for broad-spectrum diagnostics *Sens. Diagn.* **3** 203–17
- [27] Lin Z Y, He Q Y, Yin A X, Xu Y X, Wang C, Ding M N, Cheng H-C, Papandrea B, Huang Y and Duan X F 2015 Cosolvent approach for solution-processable electronic thin films *ACS Nano* **9** 4398–405
- [28] Jeong G H, Sasikala S P, Yun T, Lee G Y, Lee W J and Kim S O 2020 Nanoscale assembly of 2D materials for energy and environmental applications *Adv. Mater.* **32** 1907006
- [29] Chaves A *et al* 2020 Bandgap engineering of two-dimensional semiconductor materials *npj 2D Mater. Appl.* **4** 29
- [30] Tee B C K, Mannsfeld S C B and Bao Z N 2012 Elastomer-based pressure and strain sensors *Stretchable Electronics* ed T Someya (Wiley) pp 325–53
- [31] Saadatzi M, Saadatzi M N and Banerjee S 2020 Modeling and fabrication of a piezoelectric artificial cochlea electrode array with longitudinal coupling *IEEE Sens. J.* **20** 11163–72
- [32] Kim J *et al* 2022 All-solution-processed van der Waals heterostructures for wafer-scale electronics *Adv. Mater.* **34** 2106110
- [33] Kwon Y A *et al* 2023 Wafer-scale transistor arrays fabricated using slot-die printing of molybdenum disulfide and sodium-embedded alumina *Nat. Electron.* **6** 443–50
- [34] Lin Z Y *et al* 2018 Solution-processable 2D semiconductors for high-performance large-area electronics *Nature* **562** 254–8
- [35] Sun F Q, Lu Q F, Feng S M and Zhang T 2021 Flexible artificial sensory systems based on neuromorphic devices *ACS Nano* **15** 3875–99
- [36] Lin Z Y, Huang Y and Duan X F 2019 Van der Waals thin-film electronics *Nat. Electron.* **2** 378–88

- [37] Kovalenko M V, Scheele M and Talapin D V 2009 Colloidal nanocrystals with molecular metal chalcogenide surface ligands *Science* **324** 1417–20
- [38] Elmasry M R, Shaban S M, Elbalaawy A Y, Hafez E, Shin J, Cho S-Y and Kim D-H 2023 Fluorometric and colorimetric hybrid carbon-dot nanosensors for dual monitoring of urea *ACS Appl. Nano Mater.* **6** 7992–8003
- [39] Hu G H, Kang J, Ng L W T, Zhu X X, Howe R C T, Jones C G, Hersam M C and Hasan T 2018 Functional inks and printing of two-dimensional materials *Chem. Soc. Rev.* **47** 3265–300
- [40] Shin Y J, Ringe E, Personick M L, Cardinal M F, Mirkin C A, Marks L D, Van Duyne R P and Hersam M C 2013 Centrifugal shape sorting and optical response of polyhedral gold nanoparticles *Adv. Mater.* **25** 4023–7
- [41] Feng Y, Miyata Y, Matsuishi K and Kataura H 2011 High-efficiency separation of single-wall carbon nanotubes by self-generated density gradient ultracentrifugation *J. Phys. Chem. C* **115** 1752–6
- [42] Fagan J A, Becker M L, Chun J and Hobbie E K 2008 Length fractionation of carbon nanotubes using centrifugation *Adv. Mater.* **20** 1609–13
- [43] Protesescu L, Yakunin S, Bodnarchuk M I, Krieg F, Caputo R, Hendon C H, Yang R X, Walsh A and Kovalenko M V 2015 Nanocrystals of cesium lead halide perovskites (CsPbX₃, X = Cl, Br, and I): novel optoelectronic materials showing bright emission with wide color gamut *Nano Lett.* **15** 3692–6
- [44] Chen Y Y, Sharp D, Saxena A, Nguyen H, Cossairt B M and Majumdar A 2022 Integrated quantum nanophotonics with solution-processed materials *Adv. Quantum Technol.* **5** 2100078
- [45] Tong Y, Bohn B J, Bladt E, Wang K, Müller-Buschbaum P, Bals S, Urban A S, Polavarapu L and Feldmann J 2017 From precursor powders to CsPbX₃ perovskite nanowires: one-pot synthesis, growth mechanism, and oriented self-assembly *Angew. Chem., Int. Ed.* **56** 13887–92
- [46] Song O and Kang J 2023 Solution-processed 2D materials for electronic applications *ACS Appl. Electron. Mater.* **5** 1335–46
- [47] Kim J, Song O, Cho Y S, Jung M, Rhee D and Kang J 2022 Revisiting solution-based processing of van der Waals layered materials for electronics *ACS Mater. Au* **2** 382–93
- [48] Wang L *et al* 2020 Full-color fluorescent carbon quantum dots *Sci. Adv.* **6** eabb6772
- [49] Wu L Z *et al* 2017 Improving the stability and size tunability of cesium lead halide perovskite nanocrystals using trioctylphosphine oxide as the capping ligand *Langmuir* **33** 12689–96
- [50] Feng X M, Mao C J, Yang G, Hou W H and Zhu J-J 2006 Polyaniline/Au composite hollow spheres: synthesis, characterization, and application to the detection of dopamine *Langmuir* **22** 4384–9
- [51] Sarma T K, Chowdhury D, Paul A and Chattopadhyay A 2002 Synthesis of Au nanoparticle–conductive polyaniline composite using H₂O₂ as oxidising as well as reducing agent *Chem. Commun.* **2002** 1048–9
- [52] Miller J B, Harris J M and Hobbie E K 2014 Purifying colloidal nanoparticles through ultracentrifugation with implications for interfaces and materials *Langmuir* **30** 7936–46
- [53] Culver K S B, Shin Y J, Rotz M W, Meade T J, Hersam M C and Odum T W 2016 Shape-dependent relaxivity of nanoparticle-based T₁ magnetic resonance imaging contrast agents *J. Phys. Chem. C* **120** 22103–9
- [54] Shen J F *et al* 2015 Liquid phase exfoliation of two-dimensional materials by directly probing and matching surface tension components *Nano Lett.* **15** 5449–54
- [55] Paton K R *et al* 2014 Scalable production of large quantities of defect-free few-layer graphene by shear exfoliation in liquids *Nat. Mater.* **13** 624–30
- [56] Hernandez Y *et al* 2008 High-yield production of graphene by liquid-phase exfoliation of graphite *Nat. Nanotechnol.* **3** 563–8
- [57] Yanagi K, Miyata Y, Tanaka T, Fujii S, Nishide D and Kataura H 2009 Colors of carbon nanotubes *Diam. Relat. Mater.* **18** 935–9
- [58] Li H, Gordeev G, Garrity O, Reich S and Flavel B S 2019 Separation of small-diameter single-walled carbon nanotubes in one to three steps with aqueous two-phase extraction *ACS Nano* **13** 2567–78
- [59] Green A A and Hersam M C 2008 Colored semitransparent conductive coatings consisting of monodisperse metallic single-walled carbon nanotubes *Nano Lett.* **8** 1417–22
- [60] De S, Higgins T M, Lyons P E, Doherty E M, Nirmalraj P N, Blau W J, Boland J J and Coleman J N 2009 Silver nanowire networks as flexible, transparent, conducting films: extremely high DC to optical conductivity ratios *ACS Nano* **3** 1767–74
- [61] Sun Y G, Gates B, Mayers B and Xia Y N 2002 Crystalline silver nanowires by soft solution processing *Nano Lett.* **2** 165–8
- [62] Zhang D Q, Zhang Q P, Zhu Y Y, Poddar S, Zhang Y T, Gu L L, Zeng H B and Fan Z Y 2023 Metal halide perovskite nanowires: synthesis, integration, properties, and applications in optoelectronics *Adv. Energy Mater.* **13** 2201735
- [63] Zhu H M, Fu Y P, Meng F, Wu X X, Gong Z Z, Ding Q, Gustafsson M V, Trinh M T, Jin S and Zhu X-Y 2015 Lead halide perovskite nanowire lasers with low lasing thresholds and high quality factors *Nat. Mater.* **14** 636–42
- [64] Zhang D D, Yu Y, Bekenstein Y, Wong A B, Alivisatos A P and Yang P D 2016 Ultrathin colloidal cesium lead halide perovskite nanowires *J. Am. Chem. Soc.* **138** 13155–8
- [65] Zhang D D, Eaton S W, Yu Y, Dou L T and Yang P D 2015 Solution-phase synthesis of cesium lead halide perovskite nanowires *J. Am. Chem. Soc.* **137** 9230–3
- [66] Hu G H *et al* 2017 Black phosphorus ink formulation for inkjet printing of optoelectronics and photonics *Nat. Commun.* **8** 278
- [67] Kang J, Wells S A, Sangwan V K, Lam D, Liu X L, Luxa J, Sofer Z and Hersam M C 2018 Solution-based processing of optoelectronically active indium selenide *Adv. Mater.* **30** 1802990
- [68] Eda G, Yamaguchi H, Voiry D, Fujita T, Chen M W and Chhowalla M 2011 Photoluminescence from chemically exfoliated MoS₂ *Nano Lett.* **11** 5111–6
- [69] Jeong S, Yoo D, Ahn M, Miró P, Heine T and Cheon J 2015 Tandem intercalation strategy for single-layer nanosheets as an effective alternative to conventional exfoliation processes *Nat. Commun.* **6** 5763
- [70] Song O *et al* 2022 All inkjet-printed electronics based on electrochemically exfoliated two-dimensional metal, semiconductor, and dielectric *npj 2D Mater. Appl.* **6** 64
- [71] Hummers W S Jr and Offeman R E 1958 Preparation of graphitic oxide *J. Am. Chem. Soc.* **80** 1339
- [72] Park S, An J, Jung I, Piner R D, An S J, Li X S, Velamakanni A and Ruoff R S 2009 Colloidal suspensions of highly reduced graphene oxide in a wide variety of organic solvents *Nano Lett.* **9** 1593–7
- [73] Marciano D C, Kosynkin D V, Berlin J M, Sinitkii A, Sun Z Z, Slesarev A, Alemany L B, Lu W and Tour J M 2010 Improved synthesis of graphene oxide *ACS Nano* **4** 4806–14
- [74] Modarres M H, Kosasih F U, Ducati C and De Volder M 2019 Self-assembly of rGO coated nanorods into aligned thick films *Adv. Mater. Interfaces* **6** 1900219

- [75] Shamsi J, Dang Z Y, Bianchini P, Canale C, Di Stasio F, Brescia R, Prato M and Manna L 2016 Colloidal synthesis of quantum confined single crystal CsPbBr₃ nanosheets with lateral size control up to the micrometer range *J. Am. Chem. Soc.* **138** 7240–3
- [76] Dou L T *et al* 2015 Atomically thin two-dimensional organic-inorganic hybrid perovskites *Science* **349** 1518–21
- [77] Bekenstein Y, Koscher B A, Eaton S W, Yang P D and Alivisatos A P 2015 Highly luminescent colloidal nanoplates of perovskite cesium lead halide and their oriented assemblies *J. Am. Chem. Soc.* **137** 16008–11
- [78] Rainò G, Becker M A, Bodnarchuk M I, Mahrt R F, Kovalenko M V and Stöferle T 2018 Superfluorescence from lead halide perovskite quantum dot superlattices *Nature* **563** 671–5
- [79] Dong A G, Chen J, Vora P M, Kikkawa J M and Murray C B 2010 Binary nanocrystal superlattice membranes self-assembled at the liquid–air interface *Nature* **466** 474–7
- [80] Wang C *et al* 2018 Monolayer atomic crystal molecular superlattices *Nature* **555** 231–6
- [81] Geuchies J J *et al* 2016 *In situ* study of the formation mechanism of two-dimensional superlattices from PbSe nanocrystals *Nat. Mater.* **15** 1248–54
- [82] Liu Y *et al* 2019 Self-assembly of two-dimensional perovskite nanosheet building blocks into ordered Ruddlesden–Popper perovskite phase *J. Am. Chem. Soc.* **141** 13028–32
- [83] Qiao F, Xie Y, Weng Z K and Chu H Q 2020 Ligand engineering of colloid quantum dots and their application in all-inorganic tandem solar cells *J. Energy Chem.* **50** 230–9
- [84] Wang T Y, Zhu H C, Zhuo J Q, Zhu Z W, Papakonstantinou P, Lubarsky G, Lin J and Li M X 2013 Biosensor based on ultrasmall MoS₂ nanoparticles for electrochemical detection of H₂O₂ released by cells at the nanomolar level *Anal. Chem.* **85** 10289–95
- [85] De Volder M F L, Tawfik S H, Baughman R H and Hart A J 2013 Carbon nanotubes: present and future commercial applications *Science* **339** 535–9
- [86] Mak K F and Shan J 2016 Photonics and optoelectronics of 2D semiconductor transition metal dichalcogenides *Nat. Photon.* **10** 216–26
- [87] Mirkin C A 2000 Programming the assembly of two- and three-dimensional architectures with DNA and nanoscale inorganic building blocks *Inorg. Chem.* **39** 2258–72
- [88] Arnold M S, Stupp S I and Hersam M C 2005 Enrichment of single-walled carbon nanotubes by diameter in density gradients *Nano Lett.* **5** 713–8
- [89] Kang J, Seo J-W T, Alducin D, Ponce A, Yacaman M J and Hersam M C 2014 Thickness sorting of two-dimensional transition metal dichalcogenides via copolymer-assisted density gradient ultracentrifugation *Nat. Commun.* **5** 5478
- [90] Kang J, Sangwan V K, Wood J D, Liu X L, Balla I, Lam D and Hersam M C 2016 Layer-by-layer sorting of rhenium disulfide via high-density isopycnic density gradient ultracentrifugation *Nano Lett.* **16** 7216–23
- [91] Kang J, Sangwan V K, Wood J D and Hersam M C 2017 Solution-based processing of monodisperse two-dimensional nanomaterials *Acc. Chem. Res.* **50** 943–51
- [92] Kang J, Wells S A, Wood J D, Lee J-H, Liu X L, Ryder C R, Zhu J, Guest J R, Husko C A and Hersam M C 2016 Stable aqueous dispersions of optically and electronically active phosphorene *Proc. Natl Acad. Sci. USA* **113** 11688–93
- [93] Zhu J, Kang J, Kang J M, Jariwala D, Wood J D, Seo J-W T, Chen K-S, Marks T J and Hersam M C 2015 Solution-processed dielectrics based on thickness-sorted two-dimensional hexagonal boron nitride nanosheets *Nano Lett.* **15** 7029–36
- [94] Wei L, Flavel B S, Li W S, Krupke R and Chen Y 2017 Exploring the upper limit of single-walled carbon nanotube purity by multiple-cycle aqueous two-phase separation *Nanoscale* **9** 11640–6
- [95] Green A A and Hersam M C 2009 Solution phase production of graphene with controlled thickness via density differentiation *Nano Lett.* **9** 4031–6
- [96] Fox D W, Schropp A A, Joseph T, Azim N, Li Sip Y Y and Zhai L 2021 Uniform deposition of silver nanowires and graphene oxide by superhydrophilicity for transparent conductive films *ACS Appl. Nano Mater.* **4** 7628–39
- [97] Hosseini Z S, Iraj Zad A, Ghiass M A, Fardindoost S and Hatamie S 2017 A new approach to flexible humidity sensors using graphene quantum dots *J. Mater. Chem. C* **5** 8966–73
- [98] Pérez-Ráfols C, Bastos-Arrieta J, Serrano N, Díaz-Cruz J M, Ariño C, De Pablo J and Esteban M 2017 Ag nanoparticles drop-casting modification of screen-printed electrodes for the simultaneous voltammetric determination of Cu(II) and Pb(II) *Sensors* **17** 1458
- [99] Zahran M, Khalifa Z, Zahran M A-H and Abdel Azzem M 2020 Dissolved organic matter-capped silver nanoparticles for electrochemical aggregation sensing of atrazine in aqueous systems *ACS Appl. Nano Mater.* **3** 3868–75
- [100] Virgili A H, Laranja D C, Malheiros P S, Pereira M B, Costa T M H and de Menezes E W 2021 Nanocomposite film with antimicrobial activity based on gold nanoparticles, chitosan and aminopropylsilane *Surf. Coat. Technol.* **415** 127086
- [101] Chávez F, Pérez-Sánchez G F, Goiz O, Zaca-Morán P, Peña-Sierra R, Morales-Acevedo A, Felipe C and Soledad-Priego M 2013 Sensing performance of palladium-functionalized WO₃ nanowires by a drop-casting method *Appl. Surf. Sci.* **275** 28–35
- [102] Niu X L, Weng W J, Yin C X, Niu Y Y, Li G J, Dong R X, Men Y L and Sun W 2018 Black phosphorene modified glassy carbon electrode for the sensitive voltammetric detection of rutin *J. Electroanal. Chem.* **811** 78–83
- [103] Li X Y, Niu X L, Zhao W S, Chen W, Yin C X, Men Y L, Li G J and Sun W 2018 Black phosphorene and PEDOT: PSS-modified electrode for electrochemistry of hemoglobin *Electrochem. Commun.* **86** 68–71
- [104] Deegan R D, Bakajin O, Dupont T F, Huber G, Nagel S R and Witten T A 1997 Capillary flow as the cause of ring stains from dried liquid drops *Nature* **389** 827–9
- [105] Sun J, Zhou W H, Yang H B, Zhen X, Ma L F, Williams D, Sun X D and Lang M-F 2018 Highly transparent and flexible circuits through patterning silver nanowires into microfluidic channels *Chem. Commun.* **54** 4923–6
- [106] Jo J W, Jung J W, Lee J U and Jo W H 2010 Fabrication of highly conductive and transparent thin films from single-walled carbon nanotubes using a new non-ionic surfactant *via spin coating ACS Nano* **4** 5382–8
- [107] Torres-Rivero K, Torralba-Cadena L, Espriu-Gascon A, Casas I, Bastos-Arrieta J and Florido A 2019 Strategies for surface modification with Ag-shaped nanoparticles: electrocatalytic enhancement of screen-printed electrodes for the detection of heavy metals *Sensors* **19** 4249
- [108] Ackermann J, Reger E, Jung S, Mohr J, Hertzberg S, Seidl K and Kruss S 2024 Smart slides for optical monitoring of cellular processes *Adv. Funct. Mater.* **34** 2309064
- [109] Puetz J and Aegerter M A 2004 Dip coating technique *Sol-Gel Technologies for Glass Producers and Users* ed M A Aegerter and M Mennig (Springer) pp 37–48
- [110] Mirri F, Ma A W K, Hsu T T, Behabtu N, Eichmann S L, Young C C, Tsentelovich D E and Pasquali M 2012

- High-performance carbon nanotube transparent conductive films by scalable dip coating *ACS Nano* **6** 9737–44
- [111] Gauldin E A, Diroll B T, Goodwin E D, Vrtis Z J, Kagan C R and Murray C B 2015 Deposition of wafer-scale single-component and binary nanocrystal superlattice thin films via dip-coating *Adv. Mater.* **27** 2846–51
- [112] Aziz F and Ismail A F 2015 Spray coating methods for polymer solar cells fabrication: a review *Mater. Sci. Semicond. Process.* **39** 416–25
- [113] Pawlowski L 2009 Suspension and solution thermal spray coatings *Surf. Coat. Technol.* **203** 2807–29
- [114] Yuan J F, Bi C H, Wang S X, Guo R Q, Shen T, Zhang L X and Tian J J 2019 Spray-coated colloidal perovskite quantum dot films for highly efficient solar cells *Adv. Funct. Mater.* **29** 1906615
- [115] Mitzi D B 2009 Solution processing of chalcogenide semiconductors via dimensional reduction *Adv. Mater.* **21** 3141–58
- [116] Soni R, Joshi S R, Karmacharya M, Min H, Kim S-K, Kumar S, Kim G-H, Cho Y-K and Lee C Y 2021 Superhydrophobic and self-sterilizing surgical masks spray-coated with carbon nanotubes *ACS Appl. Nano Mater.* **4** 8491–9
- [117] Zhang S, Chen M L, Mu G, Li J M, Hao Q and Tang X 2022 Spray-stencil lithography enabled large-scale fabrication of multispectral colloidal quantum-dot infrared detectors *Adv. Mater. Technol.* **7** 2101132
- [118] Xie B L, Xu G R, Jia Y H, Gu L K, Wang Q, Mushtaq N, Cheng B W and Hu Y X 2021 Engineering carbon nanotubes enhanced hydrophobic membranes with high performance in membrane distillation by spray coating *J. Membr. Sci.* **625** 118978
- [119] Yang J *et al* 2021 Solvent engineering of colloidal quantum dot inks for scalable fabrication of photovoltaics *ACS Appl. Mater. Interfaces* **13** 36992–7003
- [120] Peng Y-Y, Akuzum B, Kurra N, Zhao M-Q, Alhabeab M, Anasori B, Kumbur E C, Alshareef H N, Ger M-D and Gogotsi Y 2016 All-MXene (2D titanium carbide) solid-state microsupercapacitors for on-chip energy storage *Energy Environ. Sci.* **9** 2847–54
- [121] Blodgett K B 1934 Monomolecular films of fatty acids on glass *J. Am. Chem. Soc.* **56** 495
- [122] Rhee S, Jung D, Kim D, Lee D C, Lee C and Roh J 2021 Polarized electroluminescence emission in high-performance quantum rod light-emitting diodes via the Langmuir–Blodgett technique *Small* **17** 2101204
- [123] Bruchiel-Spanier N and Mandler D 2015 Nanoparticle-imprinted polymers: shell-selective recognition of Au nanoparticles by imprinting using the Langmuir–Blodgett method *ChemElectroChem* **2** 795–802
- [124] Mao J, Ortiz O, Wang J J, Malinge A, Badia A and Kéna-Cohen S 2020 Langmuir–Blodgett fabrication of large-area black phosphorus-C₆₀ thin films and heterojunction photodetectors *Nanoscale* **12** 19814–23
- [125] Baratto C, Golovanova V, Faglia G, Hakola H, Niemi T, Tkachenko N, Nazarchuk B and Golovanov V 2020 On the alignment of ZnO nanowires by Langmuir–Blodgett technique for sensing application *Appl. Surf. Sci.* **528** 146959
- [126] Abdulla S and Pullithadathil B 2020 Unidirectional Langmuir–Blodgett-mediated alignment of polyaniline-functionalized multiwalled carbon nanotubes for NH₃ gas sensor applications *Langmuir* **36** 11618–28
- [127] Ariga K, Yamauchi Y, Mori T and Hill J P 2013 25th Anniversary article: what can be done with the Langmuir–Blodgett method? Recent developments and its critical role in materials science *Adv. Mater.* **25** 6477–512
- [128] Kim H, Kee J, Seo D-R, Lee Y, Ahn C W and Koo J 2020 Large-area 2D-MXene nanosheet assemblies using Langmuir–Schaefer technique: wrinkle formation *ACS Appl. Mater. Interfaces* **12** 42294–301
- [129] Kouloumpis A, Thomou E, Chalmpes N, Dimos K, Spyrou K, Bourlinos A B, Koutselas I, Gournis D and Rudolf P 2017 Graphene/carbon dot hybrid thin films prepared by a modified Langmuir–Schaefer method *ACS Omega* **2** 2090–9
- [130] Kędzierski K, Rytel K, Majchrzycki Ł and Wróbel D 2015 Conductive and transparent films of oriented multi-walled carbon nanotubes by Langmuir–Schaefer method *Thin Solid Films* **589** 701–6
- [131] Kostiuk D, Luby S, Demydenko M, Jergel M, Siffalovic P, Ivanco J and Majkova E 2016 Few-layer graphene Langmuir–Schaefer nanofilms for H₂ gas sensing *Procedia Eng.* **168** 243–6
- [132] Oliveira O N Jr, Caseli L and Ariga K 2022 The past and the future of langmuir and Langmuir–Blodgett films *Chem. Rev.* **122** 6459–513
- [133] Secor E B, Ahn B Y, Gao T Z, Lewis J A and Hersam M C 2015 Rapid and versatile photonic annealing of graphene inks for flexible printed electronics *Adv. Mater.* **27** 6683–8
- [134] Andres C M and Kotov N A 2010 Inkjet deposition of layer-by-layer assembled films *J. Am. Chem. Soc.* **132** 14496–502
- [135] Secor E B, Prabhuramirashi P L, Puntambekar K, Geier M L and Hersam M C 2013 Inkjet printing of high conductivity, flexible graphene patterns *J. Phys. Chem. Lett.* **4** 1347–51
- [136] Derby B 2010 Inkjet printing of functional and structural materials: fluid property requirements, feature stability, and resolution *Annu. Rev. Mater. Res.* **40** 395–414
- [137] Finn D J, Lotya M and Coleman J N 2015 Inkjet printing of silver nanowire networks *ACS Appl. Mater. Interfaces* **7** 9254–61
- [138] Khan S, Lorenzelli L and Dahiya R S 2015 Technologies for printing sensors and electronics over large flexible substrates: a review *IEEE Sens. J.* **15** 3164–85
- [139] Bernasconi R, Brovelli S, Viviani P, Soldo M, Giusti D and Magagnin L 2022 Piezoelectric drop-on-demand inkjet printing of high-viscosity inks *Adv. Eng. Mater.* **24** 2100733
- [140] Zhang C F *et al* 2019 Additive-free MXene inks and direct printing of micro-supercapacitors *Nat. Commun.* **10** 1795
- [141] Wu C W, Unnikrishnan B, Chen I W P, Harroun S G, Chang H T and Huang C C 2020 Excellent oxidation resistive MXene aqueous ink for micro-supercapacitor application *Energy Storage Mater.* **25** 563–71
- [142] Ahn B Y, Duoss E B, Motala M J, Guo X Y, Park S-I, Xiong Y J, Yoon J, Nuzzo R G, Rogers J A and Lewis J A 2009 Omnidirectional printing of flexible, stretchable, and spanning silver microelectrodes *Science* **323** 1590–3
- [143] Kong Y L, Tamargo I A, Kim H, Johnson B N, Gupta M K, Koh T-W, Chin H-A, Steingart D A, Rand B P and McAlpine M C 2014 3D printed quantum dot light-emitting diodes *Nano Lett.* **14** 7017–23
- [144] Zhang M M, Li L Y, Wang M J, Li T, Song K D, Nie Y and Ren B Z 2021 3D printing for biological scaffolds using poly(ionic liquid)/gelatin/sodium alginate ink *Macromol. Mater. Eng.* **306** 2100084
- [145] Wang W Z *et al* 2021 3D printing of PLA/n-HA composite scaffolds with customized mechanical properties and biological functions for bone tissue engineering *Composites B* **224** 109192
- [146] Elder B, Neupane R, Tokita E, Ghosh U, Hales S and Kong Y L 2020 Nanomaterial patterning in 3D printing *Adv. Mater.* **32** 1907142
- [147] Orangi J, Hamade F, Davis V A and Beidaghi M 2020 3D printing of additive-free 2D Ti₃C₂T_x (MXene) ink for

- fabrication of micro-supercapacitors with ultra-high energy densities *ACS Nano* **14** 640–50
- [148] Li F *et al* 2023 3D printing of inorganic nanomaterials by photochemically bonding colloidal nanocrystals *Science* **381** 1468–74
- [149] Liu X G, Shang Y H, Liu J F, Shao Z Z and Zhang C H 2022 3D printing-enabled in-situ orientation of BaTi₂O₅ nanorods in β -PVDF for high-efficiency piezoelectric energy harvesters *ACS Appl. Mater. Interfaces* **14** 13361–8
- [150] Qian Y, Li C, Qi Y Z and Zhong J 2021 3D printing of graphene oxide composites with well controlled alignment *Carbon* **171** 777–84
- [151] Jo C, Kim J, Kwak J Y, Kwon S M, Park J B, Kim J, Park G-S, Kim M-G, Kim Y-H and Park S K 2022 Retina-inspired color-cognitive learning via chromatically controllable mixed quantum dot synaptic transistor arrays *Adv. Mater.* **34** 2108979
- [152] Hou Y C, Li J D, Yoon J, Knoepfel A M, Yang D, Zheng L Y, Ye T, Ghosh S, Priya S and Wang K 2023 Retina-inspired narrowband perovskite sensor array for panchromatic imaging *Sci. Adv.* **9** eade2338
- [153] Choi C *et al* 2020 Curved neuromorphic image sensor array using a MoS₂-organic heterostructure inspired by the human visual recognition system *Nat. Commun.* **11** 5934
- [154] Kang H, Cho S-Y, Ryu J, Choi J, Ahn H, Joo H and Jung H-T 2020 Multiarray nanopattern electronic nose (E-nose) by high-resolution top-down nanolithography *Adv. Funct. Mater.* **30** 2002486
- [155] Hu N T, Yang Z, Wang Y Y, Zhang L L, Wang Y, Huang X L, Wei H, Wei L M and Zhang Y F 2014 Ultrafast and sensitive room temperature NH₃ gas sensors based on chemically reduced graphene oxide *Nanotechnology* **25** 025502
- [156] Chen Q F, Chen Z, Liu D, He Z F and Wu J M 2020 Constructing an E-nose using metal-ion-induced assembly of graphene oxide for diagnosis of lung cancer via exhaled breath *ACS Appl. Mater. Interfaces* **12** 17713–24
- [157] Jin L, Yang K, Chen L F, Yan R R, He L F, Ye M F, Qiao H B, Chu X F, Gao H and Zhang K 2023 Flexible synergistic MoS₂ quantum Dots/PEDOT: PSS film sensor for acetaldehyde sensing at room temperature *Anal. Chem.* **95** 8859–68
- [158] Lorwongtragool P, Sowade E, Watthanawisuth N, Baumann R R and Kerdcharoen T 2014 A novel wearable electronic nose for healthcare based on flexible printed chemical sensor array *Sensors* **14** 19700–12
- [159] Park S Y, Kim Y, Kim T, Eom T H, Kim S Y and Jang H W 2019 Chemoresistive materials for electronic nose: progress, perspectives, and challenges *InfoMat* **1** 289–316
- [160] Srivastava A K 2003 Detection of volatile organic compounds (VOCs) using SnO₂ gas-sensor array and artificial neural network *Sens. Actuators B* **96** 24–37
- [161] Wilson A D and Baietto M 2009 Applications and advances in electronic-nose technologies *Sensors* **9** 5099–148
- [162] Pavlou A K and Turner A P F 2000 Sniffing out the truth: clinical diagnosis using the electronic nose *Clin. Chem. Lab. Med.* **38** 99–112
- [163] Gilbertson T A, Damak S and Margolskee R F 2000 The molecular physiology of taste transduction *Curr. Opin. Neurobiol.* **10** 519–27
- [164] Wang T-H, Hui G-H and Deng S-P 2010 A novel sweet taste cell-based sensor *Biosens. Bioelectron.* **26** 929–34
- [165] Hui G-H, Mi S-S and Deng S-P 2012 Sweet and bitter tastants specific detection by the taste cell-based sensor *Biosens. Bioelectron.* **35** 429–38
- [166] Liu Q J, Zhang F N, Zhang D M, Hu N, Hsia K J and Wang P 2013 Extracellular potentials recording in intact taste epithelium by microelectrode array for a taste sensor *Biosens. Bioelectron.* **43** 186–92
- [167] Facure M H M, Schneider R, Dos Santos D M and Correa D S 2020 Impedimetric electronic tongue based on molybdenum disulfide and graphene oxide for monitoring antibiotics in liquid media *Talanta* **217** 121039
- [168] Jung H H *et al* 2023 Taste bud-inspired single-drop multitaste sensing for comprehensive flavor analysis with deep learning algorithms *ACS Appl. Mater. Interfaces* **15** 46041–53
- [169] Tan J Z and Xu J 2020 Applications of electronic nose (e-nose) and electronic tongue (e-tongue) in food quality-related properties determination: a review *Artif. Intell. Agric.* **4** 104–15
- [170] Wadehra A and Patil P S 2016 Application of electronic tongues in food processing *Anal. Methods* **8** 474–80
- [171] Lin Z Z, Zhang Q, Liu R X, Gao X J, Zhang L, Kang B Y, Shi J H, Wu Z D, Gui X J and Li X L 2016 Evaluation of the bitterness of traditional Chinese medicines using an E-tongue coupled with a robust partial least squares regression method *Sensors* **16** 151
- [172] Drake R L, Vogl A W and Mitchell A W M 2009 *Gray's Anatomy for Students E-book* 2nd edn (Churchill Livingstone)
- [173] Lan B L *et al* 2023 Multichannel gradient piezoelectric transducer assisted with deep learning for broadband acoustic sensing *ACS Appl. Mater. Interfaces* **15** 12146–53
- [174] Ahmadi H, Moradi H, Pastras C J, Abolpour Moshizi S, Wu S Y and Asadnia M 2021 Development of ultrasensitive biomimetic auditory hair cells based on piezoresistive hydrogel nanocomposites *ACS Appl. Mater. Interfaces* **13** 44904–15
- [175] Yanagihara N, Suzuki J, Gyo K, Syono H and Ikeda H 1984 Development of an implantable hearing aid using a piezoelectric vibrator of bimorph design: state of the art *Otolaryngol. Head Neck Surg.* **92** 706–12
- [176] Wang Z G, Abel E W, Mills R P and Liu Y 2002 Assessment of multi-layer piezoelectric actuator technology for middle-ear implants *Mechatronics* **12** 3–17
- [177] İlik B, Koyuncuoğlu A, Şardan-Sukas Ö and Külah H 2018 Thin film piezoelectric acoustic transducer for fully implantable cochlear implants *Sens. Actuators A* **280** 38–46
- [178] Zeng F-G, Rebscher S, Harrison W, Sun X A and Feng H H 2008 Cochlear implants: system design, integration, and evaluation *IEEE Rev. Biomed. Eng.* **1** 115–42
- [179] Briggs R J S, Eder H C, Seligman P M, Cowan R S C, Plant K L, Dalton J, Money D K and Patrick J F 2008 Initial clinical experience with a totally implantable cochlear implant research device *Otol. Neurotol.* **29** 114–9
- [180] Zeng F-G 2007 Cochlear implants: why don't more people use them? *Hear. J.* **60** 48–49
- [181] Jang J, Lee J, Jang J H and Choi H 2016 A triboelectric-based artificial basilar membrane to mimic cochlear tonotopy *Adv. Healthcare Mater.* **5** 2481–7
- [182] Liu Y Q, Li E L, Wang X M, Chen Q Z, Zhou Y L, Hu Y Y, Chen G X, Chen H P and Guo T L 2020 Self-powered artificial auditory pathway for intelligent neuromorphic computing and sound detection *Nano Energy* **78** 105403
- [183] Gong S, Yap L W, Zhu Y, Zhu B W, Wang Y, Ling Y Z, Zhao Y M, An T C, Lu Y R and Cheng W L 2020 A soft resistive acoustic sensor based on suspended standing nanowire membranes with point crack design *Adv. Funct. Mater.* **30** 1910717
- [184] Jang J, Jang J H and Choi H 2017 Biomimetic artificial basilar membranes for next-generation cochlear implants *Adv. Healthcare Mater.* **6** 1700674
- [185] Jang J *et al* 2015 A microelectromechanical system artificial basilar membrane based on a piezoelectric cantilever array and its characterization using an animal model *Sci. Rep.* **5** 12447

- [186] Lumpkin E A and Caterina M J 2007 Mechanisms of sensory transduction in the skin *Nature* **445** 858–65
- [187] Yang J C, Mun J, Kwon S Y, Park S, Bao Z N and Park S 2019 Electronic skin: recent progress and future prospects for skin-attachable devices for health monitoring, robotics, and prosthetics *Adv. Mater.* **31** 1904765
- [188] Xu J X, Ban C Y, Xiu F, Tian Z H, Jiang W J, Zhang M J, Zhang H S, Zhou Z, Liu J Q and Huang W 2021 Multimode visualization of electronic skin from bioinspired colorimetric sensor *ACS Appl. Mater. Interfaces* **13** 30205–12
- [189] Takei K, Takahashi T, Ho J C, Ko H, Gillies A G, Leu P W, Fearing R S and Javey A 2010 Nanowire active-matrix circuitry for low-voltage macroscale artificial skin *Nat. Mater.* **9** 821–6
- [190] Zhang S M, Cai L, Li W, Miao J S, Wang T Y, Yeom J, Sepúlveda N and Wang C 2017 Fully printed silver-nanoparticle-based strain gauges with record high sensitivity *Adv. Electron. Mater.* **3** 1700067
- [191] Wang B H and Facchetti A 2019 Mechanically flexible conductors for stretchable and wearable e-skin and e-textile devices *Adv. Mater.* **31** 1901408
- [192] Tao H C, Zhang Y Q, Gao Y N, Sun Z Y, Yan C and Texter J 2017 Scalable exfoliation and dispersion of two-dimensional materials—an update *Phys. Chem. Chem. Phys.* **19** 921–60
- [193] Tan C L *et al* 2017 Recent advances in ultrathin two-dimensional nanomaterials *Chem. Rev.* **117** 6225–331
- [194] Han J H, Kwak M, Kim Y and Cheon J 2018 Recent advances in the solution-based preparation of two-dimensional layered transition metal chalcogenide nanostructures *Chem. Rev.* **118** 6151–88
- [195] Konvalina G and Haick H 2012 Effect of humidity on nanoparticle-based chemiresistors: a comparison between synthetic and real-world samples *ACS Appl. Mater. Interfaces* **4** 317–25
- [196] Wei Z T, Wang J L, Liu Y H, Yuan J X, Liu T, Du G L, Zhu S Y and Nie S X 2022 Sustainable triboelectric materials for smart active sensing systems *Adv. Funct. Mater.* **32** 2208277
- [197] Yao S S, Ren P, Song R Q, Liu Y X, Huang Q J, Dong J Y, O'Connor B T and Zhu Y 2020 Nanomaterial-enabled flexible and stretchable sensing systems: processing, integration, and applications *Adv. Mater.* **32** 1902343
- [198] Rim Y S, Bae S-H, Chen H J, De Marco N and Yang Y 2016 Recent progress in materials and devices toward printable and flexible sensors *Adv. Mater.* **28** 4415–40
- [199] Jameel F, Hamid Z, Jabeen F, Zeadally S and Javed M A 2018 A survey of device-to-device communications: research issues and challenges *IEEE Commun. Surv. Tutor.* **20** 2133–68
- [200] Zhu J and Hersam M C 2017 Assembly and electronic applications of colloidal nanomaterials *Adv. Mater.* **29** 1603895
- [201] Chen B T 1983 Investigation of the solvent-evaporation effect on spin coating of thin films *Polym. Eng. Sci.* **23** 399–403
- [202] Tian C Y, Lee Y, Song Y, Elmasry M R, Yoon M, Kim D-H and Cho S-Y 2024 Machine-learning-enhanced fluorescent nanosensor based on carbon quantum dots for heavy metal detection *ACS Appl. Nano Mater.* **7** 5576–86
- [203] Cho S-Y, Lee Y, Lee S, Kang H, Kim J, Choi J, Ryu J, Joo H, Jung H-T and Kim J 2020 Finding hidden signals in chemical sensors using deep learning *Anal. Chem.* **92** 6529–37
- [204] Mukhopadhyay S C, Tyagi S K S, Suryadevara N K, Piuri V, Scotti F and Zeadally S 2021 Artificial intelligence-based sensors for next generation iot applications: a review *IEEE Sens. J.* **21** 24920–32
- [205] Vincent D R, Deepa N, Elavarasan D, Srinivasan K, Chauhdary S H and Iwendi C 2019 Sensors driven AI-based agriculture recommendation model for assessing land suitability *Sensors* **19** 3667
- [206] Cho S-Y and Jung H-T 2023 Artificial intelligence: a game changer in sensor research *ACS Sens.* **8** 1371–2
- [207] Han S, Lee Y, Kim J and Cho S-Y 2023 Physicochemical profiling of macrophage heterogeneity using deep learning integrated nanosensor cytometry *ACS Sens.* **8** 1676–83
- [208] Song Y, Tian C Y, Lee Y, Yoon M, Yoon S E and Cho S-Y 2023 Nanosensor chemical cytometry: advances and opportunities in cellular therapy and precision medicine *ACS Meas. Sci. Au* **3** 393–403